nature physics

LETTERS

https://doi.org/10.1038/s41567-020-01134-7

Check for updates

Motility-induced fracture reveals a ductile-to-brittle crossover in a simple animal's epithelia

Vivek N. Prakash[1,4], Matthew S. Bull[2] and Manu Prakash[1,3]✉

Epithelial tissues provide an important barrier function in animals, but these tissues are subjected to extreme strains during day-to-day activities such as feeding and locomotion. Understanding tissue mechanics and the adaptive response in dynamic force landscapes remains an important area of research. Here we carry out a multi-modal study of a simple yet highly dynamic organism, *Trichoplax adhaerens*, and report the discovery of abrupt, bulk epithelial tissue fractures induced by the organism's own motility. Coupled with rapid healing, this discovery accounts for dramatic shape change and physiological asexual division in this early-divergent metazoan. We generalize our understanding of this phenomenon by codifying it in a heuristic model focusing on the debonding–bonding criterion in a soft, active living material. Using a suite of quantitative experimental and numerical techniques, we demonstrate a force-driven ductile-to-brittle material transition governing the morphodynamics of tissues pushed to the edge of rupture.

Animals are characterized by their movement, and their tissues are continuously subjected to dynamic force loading while they crawl, walk, run or swim[1]. Tissue mechanics fundamentally determine the ecological niches that can be endured by a living organism[2]. Epithelial tissues are subjected to dynamic force loading and strain during several physiological processes[1,3]. However, an inability to withstand these extreme strains can result in epithelial fractures[4,5] and associated diseases[6]. From a materials science perspective, how the properties of living cells and their interactions determine larger-scale tissue rheology in dynamic force landscapes is an area of active study[7]. Tissues are the embodiment of a 'smart material'. Cells within a tissue may dynamically reconfigure under stress[8], exhibit superelastic responses by localizing strain[9], contract to actively avoid rupture[10], locally reinforce regions of tissue through recruitment[11] and exhibit other forms of mechanically regulated feedback[12]. Harnessing these properties holds promise for synthetic adaptable materials[13,14]. Many of these phenomena illustrate the role of mechanical feedback in the maintenance of tissue integrity under large strains. Here we investigate how cellular tissues behave on the threshold of failure and what determines whether a tissue fractures or flows. To this end, we examine a 'minimal tissue system' that is capable of rapid and highly adaptive plastic deformation.

We experimentally study the dynamic epithelial tissues in a marine animal, *Trichoplax adhaerens*. From a biological perspective, these early-divergent animals have a simple, flat body plan (only 25 µm in thickness but several millimetres in width), and lack a basement membrane and visible extracellular matrix[10,15–17]. Their body plan architecture consists of two distinct epithelial tissue layers (the top or upper 'dorsal' epithelium, and the bottom or lower 'ventral' epithelium, coupled at the edges[10]) which enclose a layer of fibre cells[15,16]. These animals glide on substrates using ciliary traction[18,19]. The epithelial tissues consist of millions of cells bound together solely by adherens junctions[20]. We leverage the simplicity of these animals and their flat body plan to carry out in toto imaging experiments that span many orders of magnitude in length and time scales, to gain a fundamental understanding of the plastic deformations of epithelial tissue sheets subjected to motility-induced dynamic force landscapes.

The *T. adhaerens* in our laboratory culture conditions exhibit a wide distribution of amorphous shapes and sizes (Fig. 1a and Methods). Unlike other metazoans, *T. adhaerens* does not have a fixed stereotypical adult shape. Using long-duration (about 10 h) large-field-of-view live imaging experiments, we observe that animals undergo time-dependent shape-change dynamics from more radially symmetric (circular) shapes to elongated string-like shapes (Fig. 1 and Extended Data Fig. 1). These morphological changes are essential for asexual (or 'vegetative') reproduction by fission (Fig. 1b and Supplementary Video 1), which often occurs under culture conditions[17,21].

Surprisingly, in our imaging experiments, we observe holes in both ventral and dorsal epithelial tissues, under native culture conditions. These holes are small in the beginning, grow in size and either heal completely or grow further to the size of an animal (Fig. 1c,d and Supplementary Videos 2 and 3). Sequential observation of animals reveal a continuous path from flat disk-like sheets to animals with holes (toroidal), which further break into thin, long strings (Fig. 1d and Supplementary Video 3). A contiguous tissue separating into multiple parts requires a topological transformation from a single domain to two or more isolated domains. Even for an elastic sheet this fundamentally requires plastic deformations and neighbourhood changes. Hence, we investigate these plastic deformations at both short and long timescales at cellular resolution.

We carried out live cellular-scale imaging of the ventral and dorsal tissues in open dish configurations matching native culture conditions (Fig. 2, Extended Data Fig. 2, Supplementary Video 4 and Methods). Time lapse imaging over hours reveals that the origins of these plastic events are spontaneous, localized microfractures that appear in the ventral tissue (Fig. 2a,b). These microfractures coalesce to form holes with visible cellular debris (Fig. 2b). In this context of a dissipative tissue, we observe a suppression of fracture propagation with the holes reaching a self-limiting size (Extended Data

[1]Department of Bioengineering, Stanford University, Stanford, CA, USA. [2]Department of Applied Physics, Stanford University, Stanford, CA, USA. [3]Chan Zuckerberg Biohub, San Francisco, CA, USA. [4]Present address: Department of Physics, University of Miami, Coral Gables, FL, USA. ✉e-mail: manup@stanford.edu

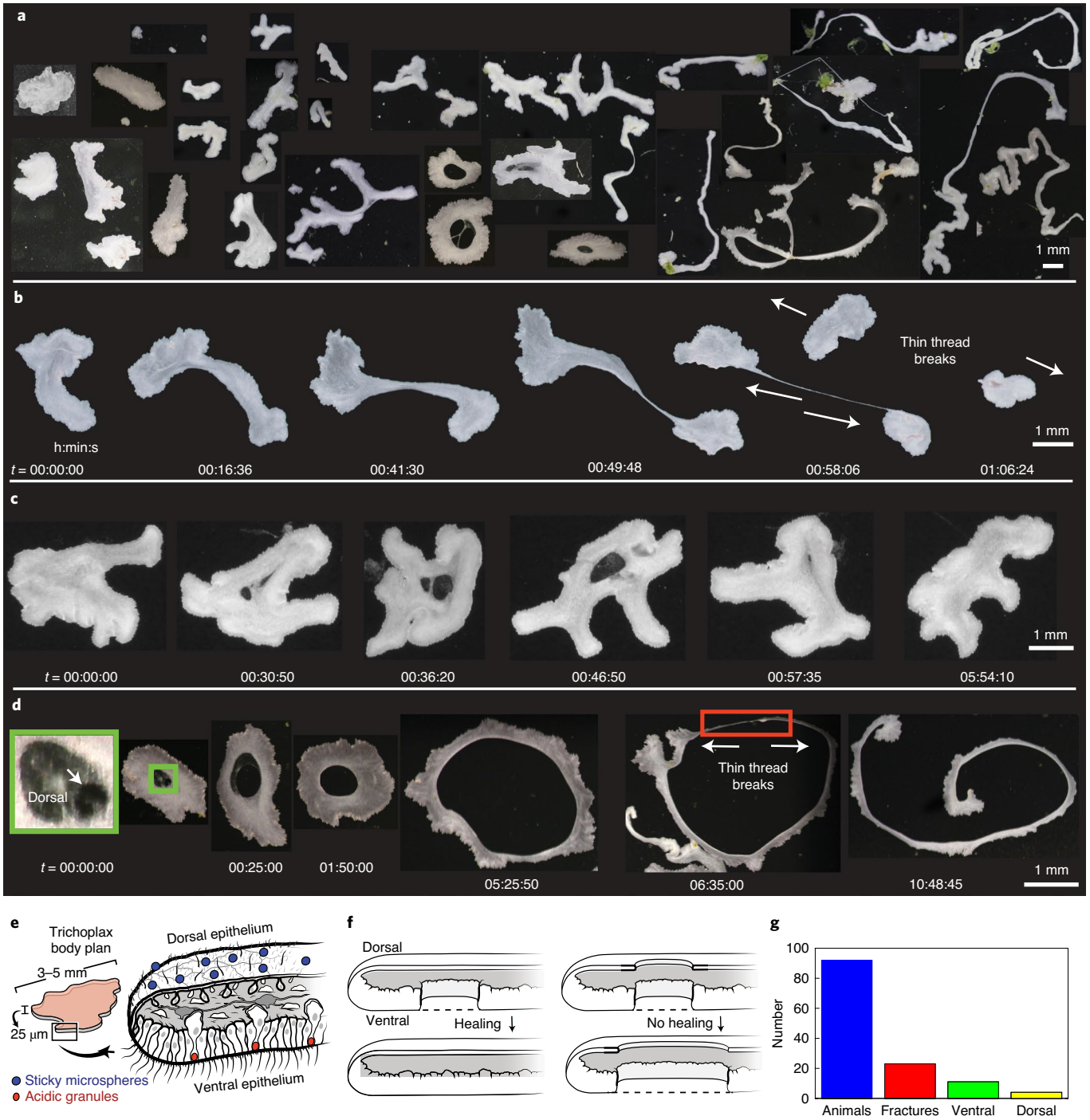

Fig. 1 | Elastic–plastic shape-change phenomena in *Trichoplax adhaerens*. **a**, Laboratory cultures show a remarkable diversity of amorphous shapes with an extreme variation in size (about 100 µm to 10 mm). **b**, Asexual reproduction by fission. Time-lapse imaging over long timescales reveals the dynamics of this shape-change process, eventually leading to asexual fission. The animal forms two regions that pull apart, resulting in a plastic shape deformation (Extended Data Fig. 1a) to produce a thin thread that is reminiscent of ductile necking. This thin thread ruptures to give rise to two daughter animals in about an hour. **c**, Ventral fracture hole initiation, propagation and healing. In the ventral epithelium, holes appear and disappear (heal) in approximately an hour (**f**). Growth via cell division takes much longer (Extended Data Fig. 1b). **d**, Dorsal fractures, threads and ruptures. In addition to ventral holes, we also observe holes in the dorsal epithelium. These dorsal holes do not heal, and lead to through holes inside the animals (**f**), which expand in cross-sectional area over time. Over time, these torodial animals further break by thread rupture and give rise to long string-like animals. A digital zoom inset is bounded by a green box to aid reader visualization. **e**, Cartoon illustrating the cross-section of the *Trichoplax* body plan and the labels we use to distinguish the dorsal and ventral epithelium (Methods). **f**, Schematic highlighting the difference between ventral fractures (left) and dorsal + ventral fractures (right). **g**, Statistics of fracture events reveal that dorsal fractures are rarer than ventral fractures (Methods).

Fig. 2a). This observation is consistent with energy arguments of fracture mechanics in plastic materials[22,23]. Individual cell mechanical heterogeneity can have a strong influence on the collective tissue mechanics[24]. Although almost bi-disperse in size distribution, the ventral tissue does not phase-separate into the two cell types (ventral epithelial cells and lipophil cells) but instead remains well

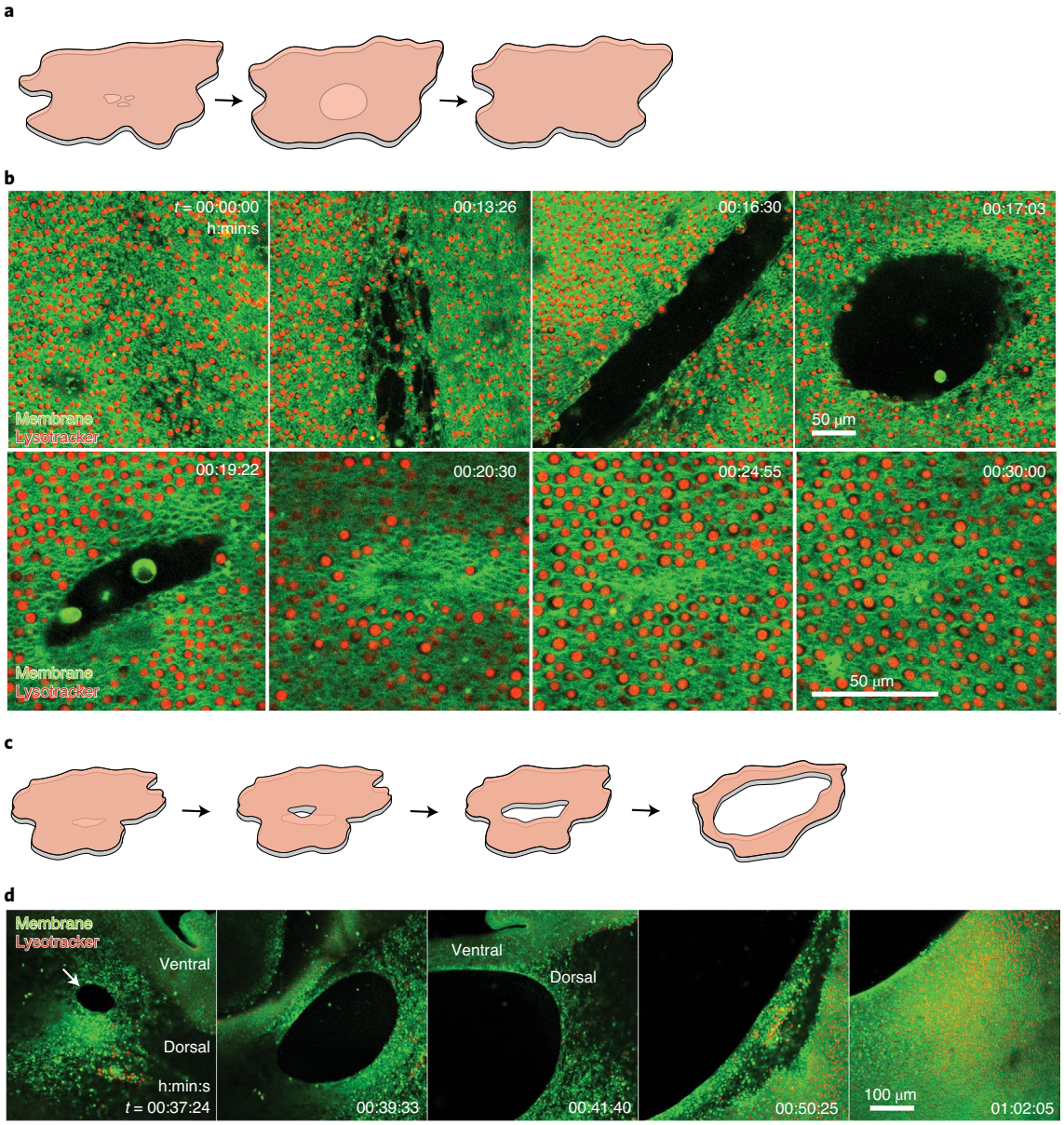

Fig. 2 | Physiological epithelial tissue fractures in the *T. adhaerens* at a cellular resolution. a, Ventral fracture hole initiation, propagation and healing. **b**, Confocal microscopy reveals that ventral layer fractures initiate as microfractures (dark regions; $N = 19$, see Methods). These coalesce to form holes with rough edges and broken fragments and further propagate to form a self-limiting larger circular hole with smooth boundaries ($N = 11$). Subsequently, the hole edges come into contact with each other, and 'healing' progresses in a zippering process to completely close the hole. **c**, Dorsal fracture hole propagation with no healing. **d**, After a ventral fracture, sometimes the dorsal layer can also sustain holes. Dorsal fractures begin as a small, smooth circular hole (white arrow) and expand in size up to the area of the ventral hole below ($N = 4$). These dorsal holes do not heal and lead to a permanent through hole inside the animal.

mixed (Supplementary Information). Remarkably, some of these fracture holes can heal completely by a zippering process at the interface of ventral epithelial cells, leaving behind a localized lipophil cell exclusion zone (Fig. 2b and Supplementary Video 5). This distribution of two cell types in the ventral tissue has a resemblance to traditional alloys in material science[25]. Borrowing from this terminology, we define an 'epithelial alloy' as a tissue characterized by multiple populations of mechanically distinct cells, and the constitutive behaviour of this epithelial alloy can be tuned by the percentage of distinct cells present.

Focusing on the dorsal epithelium reveals a entirely different phenomenon. Ventral fractures that do not heal can induce a fracture in dorsal layer (Fig. 2c). These dorsal fractures can only initiate after a corresponding ventral fracture. Unlike in the ventral layer, the dorsal tissue fracture grows quickly into a smooth circular hole similar to the size of ventral hole underneath (Fig. 2d and Extended Data Fig. 2b), akin to a ruptured elastic sheet under tension. Dorsal fractures further lead to the formation of long, narrow threads or string-like phenotypes (Fig. 1d). The dorsal fracture events are also rarer (about 4%) than the ventral fractures (about 16%) (Fig. 1g and Methods). The interface between the bulk and peripheral tissue cells can lead to fractures on the edge, and the final breaking of two ultrathin threads via extension comes down to a single cell–cell junction (Extended Data Fig. 3 and Supplementary Video 6).

Looking at the dynamics of fracture growth in dorsal versus ventral tissue, we infer distinct mechanical properties under similar

strain (Extended Data Fig. 4). This is in line with the fact that dorsal epithelium primarily consists of epithelial cells, which are 'ultrathin' and 'flat', whereas the ventral epithelium consists of a 'bi-disperse' mixture of 'columnar' epithelial cells and lipophilic cells[16] (Fig. 1e). Given that the ventral and dorsal epithelial tissue layers are coupled via an interconnected fibre cell layer, the picture of a composite tissue emerges. We can consider the properties of these tissue layers to be an integrated composite material, which is a common framework in engineered materials[26]. In the context of epithelial tissues, such a composite could permit substantial cellular stretching without breaking[9,27] or it could provide rupture resistance complemented by active response to forcing[10].

Of the models that have been used to study tissue mechanics, cell-resolved tissue models have become a powerful tool for understanding rigidity transitions[24,28–30], active tension networks[11], the importance of apical–basal symmetry breaking at the cellular level[31], how embryos generate shape[32], and the interplay of fluidity and healing of ablated wounds[33,34]. Broadly, the majority of existing models have been developed to study tissue response to slow forcing timescales in confluent monolayers with a single cell type. Our experimental observations suggest that there is more to learn about tissue mechanics by studying tissue response at unsteady and fast loading timescales (comparable to the cell–cell junction lifetime), without a confluence constraint in multi-component cellular tissues. Hence, we address here the central question of tissues under load: on short timescales, do tissues yield by fracture or by flow?

We reformulated this central question as a competition between edge-formation and neighbour exchange mediated by cell–cell junction- forming kinetics in a disordered model of an active tissue inspired by adhesive granular matter. To ground our model in experiments, we identify some key observable features that characterize epithelial tissues in *T. adhaerens*: these include cell size, cell spatial distribution, and non-confluence. Our experimental observations encouraged us to reconsider the often useful assumptions: (i) local cell mechanical uniformity, (ii) tissue confluence and (iii) the surface energy of cell–cell interactions constructed from a separation of timescales (Extended Data Fig. 5 and Methods). Also, the animal's motility arises from traction forces generated by the adherent contact of the ventral cilia on the bottom substrate, that is, the animals crawl on bottom substrates using ciliary traction[18,19].

We start with the vertex energy function for compliant adhesive cells[35], and simplify the model to replace the complexities of cell shape with an effective compliance, and also neglect cell deformation (Methods and Supplementary Information). This simplification allows us to focus on the central role of the competition between edge-forming and shear transformation zones (STZ)[36]. The mechanical properties of this model tissue will be determined by the cellular compliance and the bonding and debonding timescale, similar to ref. [28] (Methods and Supplementary Information).

A classical model for the force-dependent unbinding of two state systems (cell–cell bonding/debonding) in a tissue context follows Bell's seminal work[37]. When we study an ensemble of these two-state junctions, we find a critical behaviour where the release of one cell–cell junction redistributes that load to the others, slightly increasing the remaining junction's probability of transitioning. This induces a cascade of events that ruptures the cell–cell junctions abruptly. In the context of an elastic material, the force threshold can be translated to a geometric threshold. Approximating the cell compliance as elastic is reasonable on sufficiently short timescales[12] (Methods and Supplementary Information).

The simplest model that captures all these phenomena can be effectively characterized as a 'sticky ball-spring' model (Extended Data Fig. 5b). Cells are represented by soft circles that can deform under a Hertzian potential (Extended Data Fig. 6a). Cells are then linked through a geometrically defined dynamical network of harmonic springs when under extension. This model can be interpreted as a two-dimensional, bi-disperse, adhesive granular matter model with slow bond maturation kinetics[38] (comparable to the timescale of the dynamics). New bonds begin their maturation when they are neighbours in a Delauney triangulation and are within the geometric threshold, taking the form of a finite-distance Delauney network. Springs capture the lowest-order nonlinearity through a yield threshold: $k = k_o$ (if $\Delta l < l_{break}$) or $k = 0$ (if $\Delta l \geq l_{break}$), with $\Delta l = |r_i - r_j|$. Here, k represents the spring constant, and l_{break} represents the threshold breaking length of the spring. This is a representation of maximal strain yielding. The two cell populations of differing sizes are initialized to suppress crystallization, and the cell populations are uniformly distributed throughout the tissue using the differential adhesion hypothesis[39] (Methods and Supplementary Information).

With this heuristic framework in place, we can begin subjecting the model tissue to a controlled distributed actuation[18,19] (Methods). We conduct two primary studies of the response of this network. First, we study the model under fixed stretching for a finite time (Fig. 3a). We vary the threshold strain at which the cell–cell bonds break and sweep through a range of driving force gradients. We observe three characteristic responses. The first is the presence of a yield stress, where below a given driving amplitude, the material response is purely elastic, whereas above a certain threshold, plastic deformations are observed (Fig. 3a and Supplementary Video 7). Further, we compare our model to the classical phenomenological Herschel–Buckley model for a yield stress fluid[40], and find a good fit with a power-law scaling of about 3 (Fig. 3b) (Methods).

To classify the yielding behaviour of this model tissue, we can define a 'brittle' material as one that undergoes transformations that create new edges without STZs. A ductile response can still fracture but will do so with STZs occurring as precursors to rupture. We use this to develop a technically precise definition to characterize our ductile-to-brittle spectrum: constraint-count-conserving (CCC) transformations compare the number of constraints before and after a cell–cell neighbourhood transformation. If the number of constraints is locally conserved we call it a CCC transformation (Methods and Supplementary Information).

In the second regime, above the yield transition, we observe the tissue going through many CCC transformations in the neighbourhood matrix. These CCC transformations are analogous (though not precisely equivalent to) to T1 transformations within a tissue. This regime corresponds to ductile-like yielding transition, where cells undergo local rearrangements and only exchange their neighbours (new edges are not created). The third outcome of pulling on this model tissue is producing a large population of non-CCC transformations (the total number of 'constraints' would change), indicating the generation of boundaries. This type of yielding can be understood as a more brittle fracture via loss of tissue continuity (fractures, with new edges being created) and few associated CCC transformations to relax the energy (Methods and Supplementary Video 7).

By consolidating these results, grouped by the distributed force gradient versus debonding criteria, we can draw a phase diagram where the material undergoes the ductile-to-brittle transition above its yield stress, at a fixed value of the bi-dispersity parameters, chosen to be consistent with the actual tissue properties in the animal[16] (Fig. 3b, Extended Data Fig. 7, Supplementary Video 7 and Methods). We also varied the two key parameters controlling tissue bi-dispersity: (i) percentage of larger cells, and (ii) size ratio of large cells (Extended Data Fig. 6b(i)). However, we find a weak sensitivity to changes in the bi-dispersity on the resulting ductile-to-brittle transition (Extended Data Fig. 8).

Observing *T. adhaerens* under a microscope clearly reveals the unsteady nature of the driving force induced by its motility. Hence, we next drive this model tissue under a long wavelength collective mode akin to the unsteady dynamics observed, which captures the

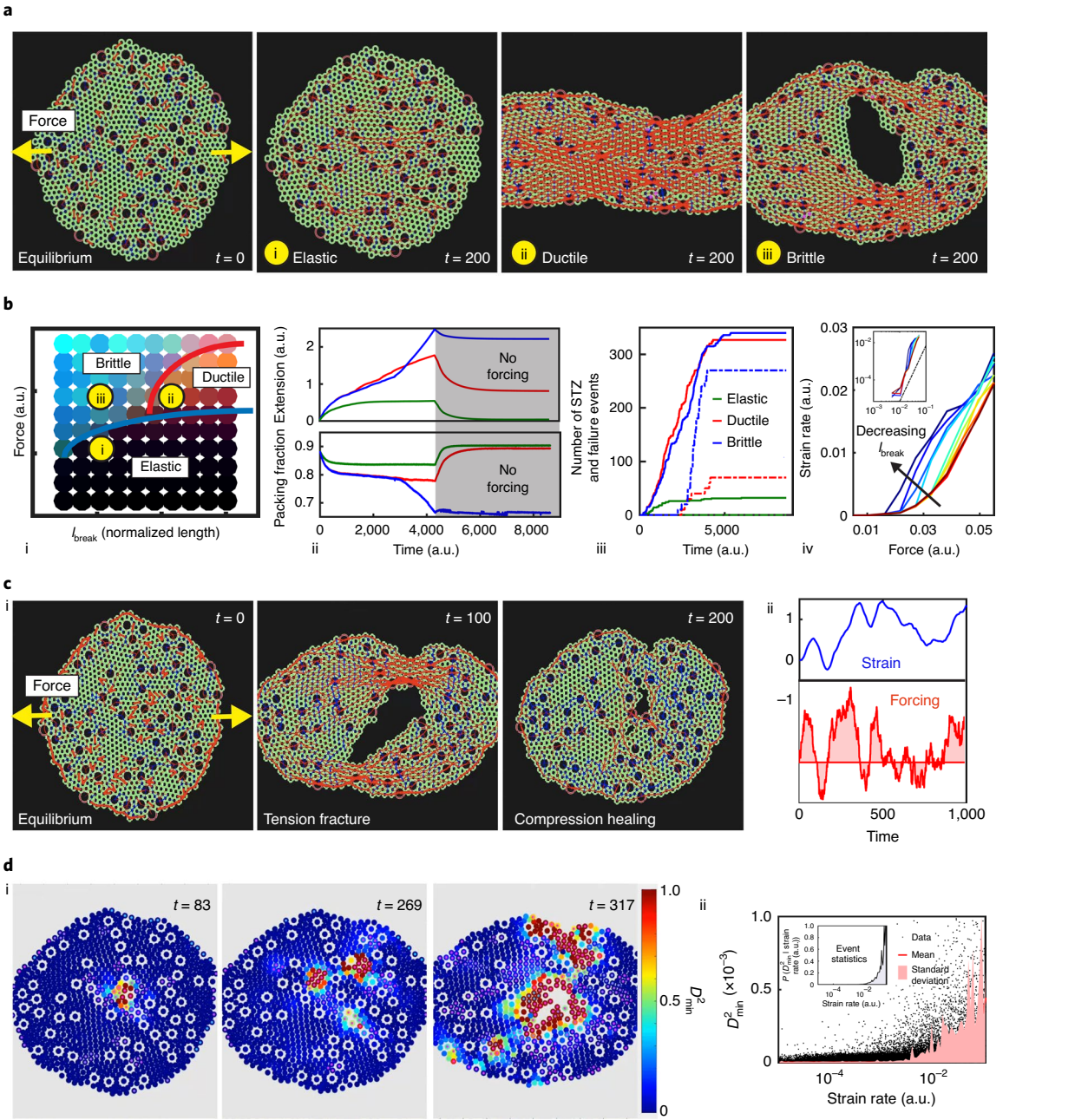

Fig. 3 | A heuristic in silico tissue model captures yielding and ductile–brittle transitions. The model consists of soft balls (of cells) connected via dynamic, compliant adhesion junctions (Methods, Extended Data Fig. 5 and Supplementary Information). **a**, Heuristic tissue model with uniform tensile loading. The system is driven out of equilibrium by a uniform tensile force gradient to mimic the lowest-order deviatoric component of distributed propulsion (yellow arrows). At low force gradients, we observe elastic behaviour (i). At high force gradients, we observe two qualitatively distinct plastic regimes, the ductile regime (ii) and the brittle regime (iii) with tissue fractures (Methods). **b**, Phase diagram of tissue properties. (i) We run a parameter sweep by varying the driving force gradient, $\nabla_x F \cdot \hat{x}$, and the strain threshold for breaking the cell–cell junctions, l_{break} ($l_{\mathrm{break}} = l/l_{\mathrm{o}}$, where l_{o} is the natural spring length), to generate a phase diagram that clearly delineates three regimes of tissue properties: elastic–ductile–brittle (Extended Data Fig. 7). (ii) At the whole-tissue scale, we characterize the response with the extension and packing fraction versus time. (iii) At the cell scale, we monitor two classes of transformations to the cell–cell connectivity associated with edge-forming transformations (dotted line) and constraint-count-conserving transformations (solid line) akin to STZs (Methods). (iv) The steady-state response of each parameter set is consistent with the Herschel–Buckley response with a finite yield stress and a scaling of 3. Inset: log–log plot showing a slope of 3. **c**, Tissue model with non-uniform/unsteady loading. (i) To investigate the role of dynamic loading, the model is driven by non-uniform, unsteady, fluctuating forces with a characteristic timescale (ii) reminiscent of locomotion in *T. adhaerens* (Methods). This time-varying force landscape captures both tissue fracture and healing dynamics. **d**, Non-affine motion analysis. (i) To identify experimentally accessible measurements of yielding, we carry out a non-affine motion analysis using the metric (D^2_{min}) (ref. [36]) on the simulations (Methods). (ii) The probability of high non-affine motion (D^2_{min}) plotted against the instantaneous strain rate highlights signatures consistent with a yield stress behaviour. Inset: probability of D^2_{min} above a threshold strain rate. All times t are in simulation units.

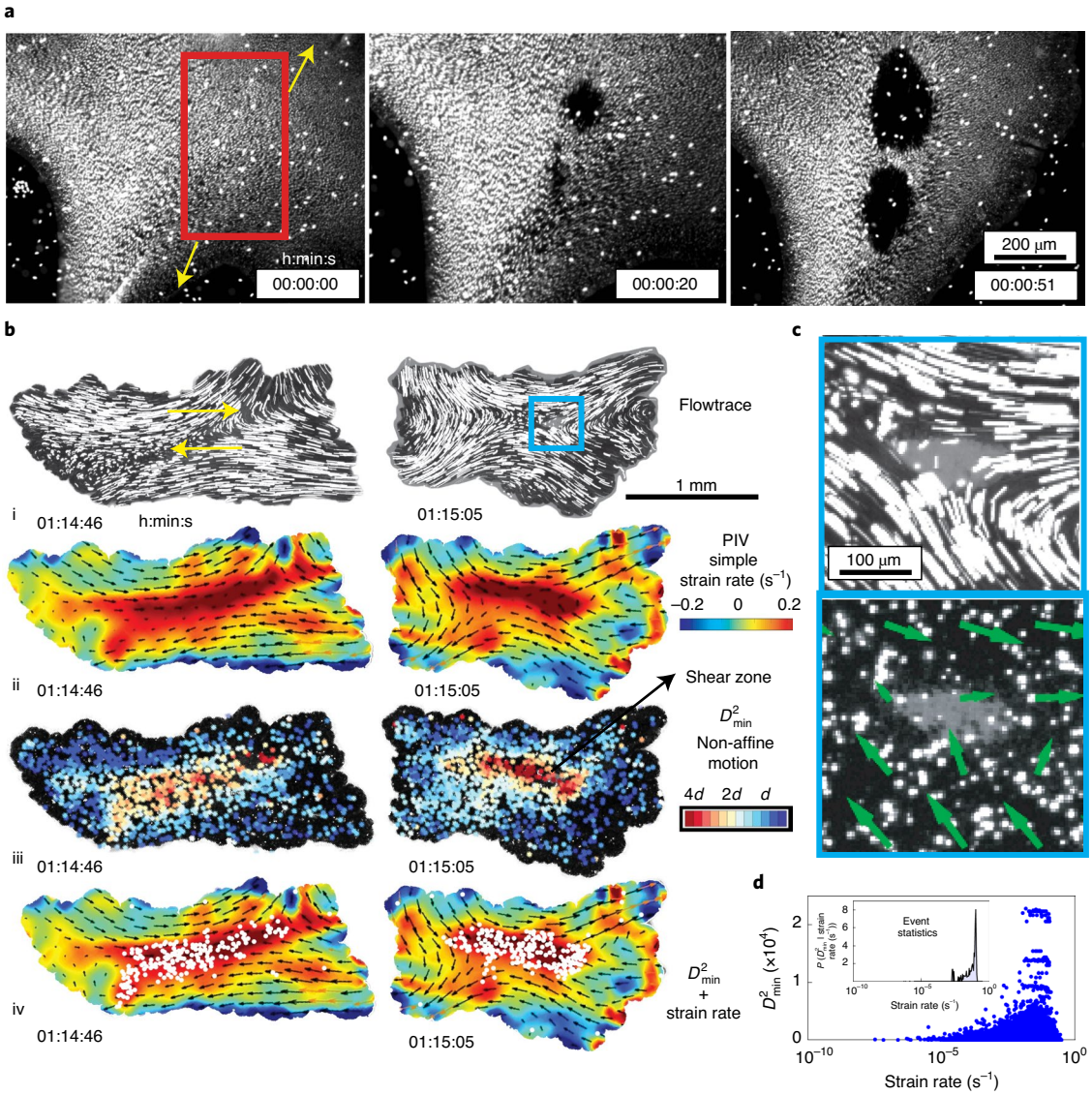

Fig. 4 | Organismal motility-induced forces cause local tissue fractures in *T. adhaerens*. a, Tension-induced epithelial fracture. Fluorescence microscopy reveals that tensile forces can induce fast (about 2 min) brittle-like fracture dynamics in the ventral epithelium (Extended Data Fig. 10 and Methods). Microfractures rapidly coalesce to form larger holes. Red box, region where tissue fractures; yellow arrows, tensile forces. **b**, Shear-induced epithelial fracture. While simultaneously imaging sticky fluorescent microbeads on the dorsal epithelium (Supplementary Fig. 1 and Supplementary Information), we observe a shear-induced ventral fracture. (i) Flowtrace[42] visualizations reveal bead trajectories in a region of local shear-induced fracture (see zoomed-in insets in **c**). Blue box, region highlighted in zoomed-in panel **c**. (ii) The internal strain rate (with peak at around 0.2 s^{-1}) contours from a PIV analysis overlaid on the velocity vectors. (iii) Non-affine motion analysis metric D^2_{min} (ref. [36]) captures high shear transformations (Methods). *d* represents the length scale of a single dorsal epithelial cell. (iv) Regions of high D^2_{min} (white dots) show excellent correlation with regions of high internal strain (red contours). **c**, Top: flowtrace visualization. Bottom: velocity vectors (green arrows). **d**, Tissue is a yield-stress material. Quantification of D^2_{min} versus the strain rate demonstrates signatures of a yield-stress material, which is consistent with model predictions (Fig. 3d). Inset: probability of D^2_{min} above a threshold strain rate.

self-inflicted rheology of the tissue. We implement this by varying the pulling amplitude in time using a one-dimensional random walk in a soft harmonic potential. Under such unsteady loading, the model tissue captures both fractures and healing (Fig. 3c, Supplementary Video 8 and Methods).

We can leverage the the model's direct access to the microstates to quantify changes to the connectivity matrix of the cells to arrive at experimentally observable parameters. This capability allows us to identify relationships between connectivity changing events and locally non-affine motion. Existing metrics for quantification of non-affine motion such as D^2_{min} (ref. [36]) excel at capturing the localization of STZs in space and time. This D^2_{min} metric quantifies the amount of disorder in the particle motion (Extended Data Fig. 9 and Methods). The localized STZ quantified by the D^2_{min} form a compelling measurement of dynamical heterogeneity[41], and we exploit these signatures to provide support for a finite yield stress within the tissue. We find that D^2_{min} is an excellent indicator of the connectivity-changing events (both CCC and non-CCC) (Fig. 3d). Next, we find that the yield stress character of this tissue manifests itself as an abrupt rise in the correlational measure between D^2_{min} (measure of STZ) and the instantaneous strain rate (Fig. 3d).

Inspired by our in silico tissue model results, we turn back to experiments to further understand how forces govern tissue mechanics. To perform quantitative measurements in live epithelial tissues under native conditions, we developed cell-tagging techniques and computational data analysis techniques[42] (Supplementary Fig. 1 and Supplementary Information). As suggested by our model, the experiments indeed confirm that organism-scale motile forces can give rise to brittle-like tissue fractures (Fig. 4).

The principal modes by which materials fail by fracture are classified as tensile failure (mode I), shear failure (mode II) and failure due to out-of-plane tearing (mode III)[23]. We find experimental evidence of the first two failure modes in the tissues of *T. adhaerens*: a tension-induced failure (mode I) (Fig. 4a, Extended Data Fig. 10 and Supplementary Video 9) and a shear-induced failure (mode II) (Fig. 4b,c, Supplementary Video 10 and Methods). In our experiments, we do not observe the third failure mode (mode III) because the forcing is confined to a two-dimensional plane.

Next, we proceed to investigate the material properties of these tissues. To do this, we first experimentally measure the amount of plastic deformation (shear transformations) in the tissues using the non-affine deformation metric D^2_{min} (ref. [36]) (Fig. 4b, Supplementary Video 11 and Methods), encouraged by its success in our model above. Second, we measure the internal strain rate (typically 20% s^{-1}; with maximal rupture strain around 300%) induced in the tissues by the animal's own motility (Supplementary Fig. 2, Methods and Supplementary Information). We find a high degree of correlation between these measures of plastic deformation and internal strain rate (Fig. 4b and Supplementary Video 12). In both our experiments (Fig. 4d) and model (Fig. 3d), we observe an abrupt rise in the D^2_{min} versus strain rate plot, which strongly suggests that these epithelial tissues exhibit properties of yield stress materials both with and without new-edge formation. Our measurements compare well with other yield stress phenomena in biological tissues, including zebrafish embryos[43] (about 75% linear strain) or in cell culture systems[9] (about 300% areal strain).

We have so far observed that the *T. adhaerens* experiences loading at fast timescales. Our model reveals that under such fast loading timescales (relative to cell–cell maturation time τ_{mature}), otherwise ductile tissues can become brittle because new cell–cell bonds are still fragile (Extended Data Fig. 7). It is therefore noteworthy that a tissue under such fast loading can yield by flow, in contrast to yielding by fracture. This suggests that *T. adhaerens* might have tuned its tissue properties via making epithelial alloys and composite architecture. Our observations of the ductile characteristics of the dorsal layer and brittle-like properties of the ventral layer further support this idea. While we have primarily focused on fast-timescale dynamics (seconds), we have neglected the longer-timescale (hours) effects of growth via cell division, which will also play a part in longer-term tissue shape changing and deformation[44] (Extended Data Fig. 1).

The rich and diverse dynamics of a living tissue can be interpreted through many complementary viewpoints, each with useful insights. Here we have suggested a perspective combining adhesive granular matter and concepts from materials science to study the fast-timescale dynamics of epithelial tissues under distributed loading. We report the utility of this approach to inform the generic aspects of the yielding behaviour of cellularized tissues, and the competition between fracture and flow. This perspective complements a broader trend in the biological physics of tissues[9,11,29,43–49].

Living materials such as epithelial alloys arise from repeated evolutionary trial and error. On evolutionary timescales, epithelial alloys may allow for tuning of the emergent mechanics of tissues to avoid catastrophic failure. Here we have observed how tissues can localize damage by increasing dissipation and by the ability to heal rapidly. This resilience to failure modes can expand the ecological niches in which organisms can thrive, enabling the early divergent *T. adhaerens* to successfully populate tropical oceans worldwide[50].

Online content

Any methods, additional references, Nature Research reporting summaries, source data, extended data, supplementary information, acknowledgements, peer review information; details of author contributions and competing interests; and statements of data and code availability are available at https://doi.org/10.1038/s41567-020-01134-7.

Received: 2 April 2020; Accepted: 27 November 2020;
Published online: 18 January 2021

References

1. Fung, Y. *Biomechanics: Motion, Flow, Stress, and Growth* (Springer, 1990).
2. Denny, M. W. *Ecological Mechanics: Principles of Life's Physical Interactions* 1st edn (Princeton Univ. Press, 2017).
3. Carter, J. A., Hyland, C., Steele, R. E. & Collins, E. M. S. Dynamics of mouth opening in hydra. *Biophys. J.* **110**, 1191–1201 (2016).
4. Casares, L. et al. Hydraulic fracture during epithelial stretching. *Nat. Mater.* **14**, 343–351 (2015).
5. Harris, A. R. et al. Characterizing the mechanics of cultured cell monolayers. *Proc. Natl Acad. Sci. USA* **109**, 16449–16454 (2012).
6. Vlahakis, N. E. & Hubmayr, R. D. Response of alveolar cells to mechanical stress. *Curr. Opin. Critical Care* **9**, 2–8 (2003).
7. Xi, W., Saw, T. B., Delacour, D., Lim, C. T. & Ladoux, B. Material approaches to active tissue mechanics. *Nat. Rev. Mater.* **4**, 23–44 (2019).
8. David, R. et al. Tissue cohesion and the mechanics of cell rearrangement. *Development* **141**, 3672–3682 (2014).
9. Latorre, E. et al. Active superelasticity in three-dimensional epithelia of controlled shape. *Nature* **563**, 203–208 (2018).
10. Armon, S., Bull, M. S., Aranda-Diaz, A. & Prakash, M. Ultrafast epithelial contractions provide insights into contraction speed limits and tissue integrity. *Proc. Natl. Acad. Sci. USA* **115**, E10333–E10341 (2018).
11. Noll, N., Mani, M., Heemskerk, I., Streichan, S. J. & Shraiman, B. I. Active tension network model suggests an exotic mechanical state realized in epithelial tissues. *Nat. Phys.* **13**, 1221–1226 (2017).
12. Khalilgharibi, N. et al. Stress relaxation in epithelial monolayers is controlled by the actomyosin cortex. *Nat. Phys.* **15**, 839–847 (2019).
13. Matsuda, T., Kawakami, R., Namba, R., Nakajima, T. & Gong, J. P. Mechanoresponsive self-growing hydrogels inspired by muscle training. *Science* **363**, 504–508 (2019).
14. Cordier, P., Tournilhac, F., Soulié-Ziakovic, C. & Leibler, L. Self-healing and thermoreversible rubber from supramolecular assembly. *Nature* **451**, 977–980 (2008).
15. Schierwater, B. & DeSalle, R. Placozoa. *Curr. Biol.* **28**, R97–R98 (2018).
16. Smith, C. et al. Novel cell types, neurosecretory cells, and body plan of the early-diverging metazoan *Trichoplax adhaerens*. *Curr. Biol.* **24**, 1565–1572 (2014).
17. Srivastava, M. et al. The *Trichoplax* genome and the nature of placozoans. *Nature* **454**, 955–960 (2008).
18. Bull, M., Armon, S., Prakash, V. N. & Prakash, M. The dynamics of multi-cellular coordination in a living fossil. *Bull. Am. Phys. Soc.* **2018**, B51.004 (2018).
19. Smith, C. L., Reese, T., Govezensky, T. & Barrio, R. A. Coherent directed movement towards food modeled in *Trichoplax*, a ciliated animal lacking a nervous system. *Proc. Natl. Acad. Sci. USA* **116**, 8901–8908 (2019).
20. Smith, C. L. & Reese, T. S. Adherens junctions modulate diffusion between epithelial cells in *Trichoplax adhaerens*. *Biol. Bull.* **231**, 216–224 (2016).
21. Eitel, M., Guidi, L., Hadrys, H., Balsamo, M. & Schierwater, B. New insights into placozoan sexual reproduction and development. *PLoS ONE* **6**, e19639 (2011).
22. Griffith, A. A. The phenomena of rupture and flow in solids. *Phil. Trans. R. Soc. A* **221**, 163–198 (1921).
23. Anderson, T. L. *Fracture Mechanics: Fundamentals and Applications* (CRC Press, 2017).
24. Li, X., Das, A. & Bi, D. Mechanical heterogeneity in tissues promotes rigidity and controls cellular invasion. *Phys. Rev. Lett.* **123**, 058101 (2019).
25. Callister, W. D. & Rethwisch, D. G. *Materials Science and Engineering: An Introduction* 9th edn (Wiley, 2014).
26. Lee, N., Robinson, J. & Lu, H. Biomimetic strategies for engineering composite tissues. *Curr. Opin. Biotechnol.* **40**, 64–74 (2016).
27. Burla, F., Tauber, J., Dussi, S., van der Gucht, J. & Koenderink, G. H. Stress management in composite biopolymer networks. *Nat. Phys.* **15**, 549–553 (2019).
28. Czirok, A. & Isai, D. G. Cell resolved, multiparticle model of plastic tissue deformations and morphogenesis. *Phys. Biol.* **12**, 016005 (2015).
29. Bi, D., Lopez, J. H., Schwarz, J. M. & Manning, M. L. A density-independent rigidity transition in biological tissues. *Nat. Phys.* **11**, 1074–1079 (2015).

30. Merkel, M., Baumgarten, K., Tighe, B. P. & Manning, M. L. A minimal-length approach unifies rigidity in underconstrained materials. *Proc. Natl Acad. Sci. USA* **116**, 6560–6568 (2019).
31. Nissen, S. B., Rønhild, S., Trusina, A. & Sneppen, K. Theoretical tool bridging cell polarities with development of robust morphologies. *eLife* **7**, e38407 (2018).
32. Fletcher, A. G., Osterfield, M., Baker, R. E. & Shvartsman, S. Y. Vertex models of epithelial morphogenesis. *Biophys. J.* **106**, 2291–2304 (2014).
33. Tetley, R. J. et al. Tissue fluidity promotes epithelial wound healing. *Nat. Phys.* **15**, 1195–1203 (2019).
34. Zulueta-Coarasa, T. & Fernandez-Gonzalez, R. Dynamic force patterns promote collective cell movements during embryonic wound repair. *Nat. Phys.* **14**, 750–758 (2018).
35. Nagai, T. & Honda, H. A dynamic cell model for the formation of epithelial tissues. *Phil. Mag. B* **81**, 699–719 (2001).
36. Falk, M. L. & Langer, J. S. Dynamics of viscoplastic deformation in amorphous solids. *Phys. Rev. E* **57**, 7192–7205 (1998).
37. Bell, G. I. Models for the specific adhesion of cells to cells. *Science* **200**, 618–627 (1978).
38. Koeze, D. J. & Tighe, B. P. Sticky matters: jamming and rigid cluster statistics with attractive particle interactions. *Phys. Rev. Lett.* **121**, 188002 (2018).
39. Manning, M. L., Foty, R. A., Steinberg, M. S. & Schoetz, E.-M. Coaction of intercellular adhesion and cortical tension specifies tissue surface tension. *Proc. Natl Acad. Sci. USA* **107**, 12517–12522 (2010).
40. Bonn, D., Denn, M. M., Berthier, L., Divoux, T. & Manneville, S. Yield stress materials in soft condensed matter. *Rev. Mod. Phys.* **89**, 035005 (2017).
41. Dauchot, O., Marty, G. & Biroli, G. Dynamical heterogeneity close to the jamming transition in a sheared granular material. *Phys. Rev. Lett.* **95**, 265701 (2005).
42. Gilpin, W., Prakash, V. N. & Prakash, M. Flowtrace: simple visualization of coherent structures in biological fluid flows. *J. Exp. Biol.* **220**, 3411–3418 (2017).
43. Mongera, A. et al. A fluid-to-solid jamming transition underlies vertebrate body axis elongation. *Nature* **561**, 401–405 (2018).
44. Wyatt, T., Baum, B. & Charras, G. A question of time: tissue adaptation to mechanical forces. *Curr. Opin. Cell Biol.* **38**, 68–73 (2016).
45. Armon, S., Bull, M. S., Moriel, A., Aharoni, H. & Prakash, M. Epithelial tissues as active solids: from nonlinear contraction pulses to rupture resistance. *bioRxiv* https://doi.org/10.1101/2020.06.15.153163 (2020).
46. Kim, S., Pochitaloff, M., Stooke-Vaughan, G. & Campas, O. Embryonic tissues as active foams. *bioRxiv* https://doi.org/10.1101/2020.06.17.157909 (2020).
47. Krajnc, M. Solid–fluid transition and cell sorting in epithelia with junctional tension fluctuations. *Soft Matter* **16**, 3209–3215 (2020).
48. Charras, G. & Yap, A. S. Tensile forces and mechanotransduction at cell–cell junctions. *Curr. Biol.* **28**, R445–R457 (2018).
49. Park, J. A. et al. Unjamming and cell shape in the asthmatic airway epithelium. *Nat. Mater.* **14**, 1040–1048 (2015).
50. Pearse, V. B. & Voigt, O. Field biology of placozoans (*Trichoplax*): distribution, diversity, biotic interactions. *Integr. Comp. Biol.* **47**, 677–692 (2007).

Publisher's note Springer Nature remains neutral with regard to jurisdictional claims in published maps and institutional affiliations.

© The Author(s), under exclusive licence to Springer Nature Limited 2020

Methods

Laboratory cultures of *T. adhaerens* and marine algae. We maintain laboratory cultures of *T. adhaerens* (gift from L. Buss, Yale University) in shelves of Petri dishes containing artificial seawater (ASW) in a dedicated room maintained at 19 °C temperature with an 18 h light and 6 h dark cycle. The ASW is prepared by adding measured quantities of Kent Marine Reef Salt mix in Millipore water on a magnetic stirrer in order to reach a salinity of 3%. The salinity is measured using a handheld salinity probe (CDH45, Omega Engineering). The food source for *T. adhaerens* is the marine alga *Rhodomonas lens*. We maintain separate axenic cultures of R-lens in ASW inside 500-ml Erlenmeyer flasks in dedicated incubators maintained at 14 °C. The algae are provided with nutrients (Micro Algae Grow, Florida Aqua Farms) and an 18 h light and 6 h dark cycle for optimum growth. We carry out regular maintenance of the animal and algae cultures once every week. We prepare fresh plates by filling three-fourths the volume of a petri dish with fresh ASW and algae nutrients (250 µl nutrient per litre of ASW). We then seed these fresh plates with about 5–10 ml of *R. lens* algae and let the plates grow an algae biofilm for 1–2 days. After this, we transfer about 20–30 animals from another slightly older dish and let the animals settle down and grow. The ASW in older plates of *T. adhaerens* are replaced every week (2/3 volume) with fresh ASW, algae nutrients and a few millilitres of *R. lens* algae. The axenic algae cultures are split once every week; 50 ml of algae from an older flask is transferred into 200 ml of fresh ASW and nutrients (with concentration of 500 µl nutrients per litre of ASW). These axenic algae culture flasks are shaken regularly at least once every day.

Live imaging and microscopy experiments. For long-term imaging studies (Fig. 1), the laboratory culture Petri dishes containing *T. adhaerens* are placed on a base of a modified Stereomicroscope (Leica S9 D) stand; where a digital single-lens reflex camera (Canon EOS Rebel T3i) fitted with a zoom lens (Canon EF lens 24-105 mm) replaces the stereo-zoom optical magnification unit. The imaging system employs a quasi-dark-field setting and high-resolution images are acquired remotely on a computer once every 5 s.

The animals in culture dishes adhere to the bottom surface, and we gently impinge them with small water jets from the side repeatedly using micropipettes to peel them off the surface and transfer them elsewhere for imaging. Depending on the type of experiment, we carry out live imaging of the animals by transferring them into different imaging chambers. We employed chambered coverglass wells: Nunc Lab-Tek chambers (1-well, Thermo Fisher Scientific); this configuration allows imaging of the animals under natural conditions without any confinement. We then stain the animals with fluorescent labels and carry out live confocal imaging (Zeiss LSM 780 and 880) for many hours, using minimum laser intensity (1–5%) and an acquisition rate of 2 fps, with some variation in acquisition rate depending on objective used (10× air, 20× air, 25× water, 40× oil). In these live confocal microscopy experiments, the imaging objective was looking at the animals from below, that is, by primarily focusing on the ventral epithelium. A ventral fracture hole actually enabled us to change the z-plane to go through the animal and also focus on the dorsal epithelium. In Extended Data Fig. 2, when we focus on the ventral fracture hole (in A), the dorsal epithelium is out of focus, and vice versa when we focus on dorsal holes (in Extended Data Fig. 2b).

We also carried out imaging in custom-designed PDMS milli-fluidic hexagonal chambers (thickness 40 µm, widths 1–3 mm); these chambers confine the animal movements in z-direction, and allow motility only in the two-dimensional x–y plane, depending on the width of the chambers. Once the animals have settled down in the imaging chambers (over hours) and the chambers are sealed, they are mounted on an inverted microscope (Nikon TE2000-U) and imaged under bright field and fluorescence (lambda XL light source) modalities. The images are captured using on a high-speed camera (ORCA Flash 4.0, Hamamatsu) generally at frame rates of 10 fps for long durations (many hours), but the frame rates and durations are varied in some specific experiments. Depending on the particular experiment's objective to achieve specific fields of view, different objectives were used for imaging: 2×, 4×, 10× and 60× oil immersion objectives.

Statistics of fracture events in experiments. In Fig. 1g, we show the statistics of fracture events in a bar chart. These fracture statistics are based on the fracture events that we were able to record. These statistics represent only a lower bound since these events are continuous processes in these animals; we were not able to capture all events (especially when they occur overnight). Here, we imaged a total number of animals $N = 92$, of size 2 mm and larger in our confocal microscopy experiments. The number of fracture events is $N = 42$ (including microfractures, thread fractures, ventral fractures and dorsal fractures). The number of ventral fractures that healed is $N = 11$, and the number of ventral fractures that led to dorsal fractures is $N = 4$. The dorsal fracture events are rarer (about 4%) than the ventral fractures (about 16%).

Heuristic in silico model of ventral epithelial tissue. A good starting point for compliant adhesive cells is the vertex energy function[35], where we unfold the surface tension-like term into the contribution coming from cortical tension and the contribution coming from interaction with other sticky cells[39,48,51]. Since the dynamics we study overlaps with the timescales of the cell–cell bond lifetime, we split the second term of cell–cell interaction energy into the dynamics of adhesive bonds. The energy function for a unit cell i is given by:

$$\epsilon_i = k_A(A_i - A_{i,o})^2 + \Gamma P_i^2 + \alpha_i P_i + \sum_j \delta_{i,j}\Sigma(\tau_{i,j})$$

where k_A and Γ are the areal (A) and perimeter (P) rigidity respectively, α is the cell's cortical tension, $\delta_{i,j}$ is a dynamical term counting the number of cell–cell junctions present and bound between cell's i and j where we sum over all the cells in contact with cell i. $\Sigma(\tau_{i,j})$ is the energy of a cell–cell junction, which can be age-dependent, $\tau = t - t_{\text{creation}}$ (if the timescale of the formation dynamics is comparable to the timescale of study). Here we assume that $\Sigma(\tau) \approx 1 - e^{\tau/T_c}$ where T_c is the characteristic timescale of bond formation.

A classical model for the force-dependent unbinding of two state systems (cell–cell bonding/debonding) in a tissue context follows Bell's seminal work[37]. When we study an ensemble of these two-state junctions, we find a critical behaviour where the release of one cell–cell junction redistributes that load to the others, slightly increasing the remaining junction's probability of transitioning. This induces a cascade of events which ruptures the cell–cell junctions abruptly. We find that for sufficiently high affinities and ensemble sizes, the collective dynamics is well approximated by a Heaviside step (Supplementary Information):

$$\sum_j \delta_{i,j} = \langle n_{\text{bound}}\rangle(F_{\text{pull}}) \approx |N(t)P_{\text{ss}}|_{\langle F\rangle\to 0}\left(1 - \Theta_{\text{Heaviside}}(F_{\text{pull}} - F_c)\right)$$

where $\langle n_{\text{bound}}\rangle$ is the average number of bound junctions, F_{pull} is the average pull force, $N(t)$ is the number of local cadherins clustering[52,53] (timescale about 10 s), and F_c is the critical failure force. $N(t)$ is the limiting timescale of our proposed bonding criterion. We define this timescale as the maturation time τ_{mature} of the cell–cell junction[54] and is precisely related to the term in our energy function above $\Sigma(\tau) = \sigma N(\tau)$, where σ is the energy of a single cell–cell junction. In the context of an elastic material, the force threshold can be translated to a geometric threshold. Approximating the cell compliance as elastic is reasonable on sufficiently short timescales[12].

Given these complexities in tissue mechanics, we choose the simplest model that focuses our attention on the new representation: cell–cell bonding/debonding criteria. The simplest model that captures these phenomena can be effectively characterized as a 'sticky ball-spring' model (Extended Data Fig. 5). Cells are represented by soft circles that can deform under a Hertzian potential. Cells are then linked through a geometrically defined dynamical network of harmonic springs when under extension. The two populations of cells of different sizes are initialized to suppress crystallization (consistent with experimental observations). To ensure that the cell populations are uniformly distributed throughout the tissue, we leverage the differential adhesion hypothesis[39] encoded through attachment stiffness between cell types. By choosing the correct relationship, $k_{22} < k_{11} < k_{12}$, cells will preferentially distribute throughout the tissue when rapidly quenched from a random initial state (but not an infinite–temperature quench). The quench dynamics take the form of a gradient descent on the energy landscape with the dynamical equation:

$$\gamma\frac{\partial}{\partial t}r_i = -\nabla_{r_i}\sum_k \epsilon_k(r_1, ..., r_{2N}) + \xi(t)$$

The gradients are taken analytically and the positions are updated using a combination of Euler's method and a custom variant of a fast inertial relaxation engine.

The number of metastable states in the model tissues explodes rapidly with increased bidispersity via size and percentage of large cells, reminiscent of a collodial glass. In an ensemble of these metastable states, we can study the packing fraction, the hexatic order and the residual force as a function of the size difference between cells and the percentage of each cell population. We set these to be consistent with experimental measurements and observe similar observables, including the orientational correlation length of the hexatic order parameter (Extended Data Fig. 6). Even though our model does not have viscoelastic components, we find the emergent bulk viscoelasticity at finite temperature through neighbourhood exchanges to be consistent with many yield stress fluids[40].

A classic phenomenological model for a yield stress fluid is captured by the Herschel–Buckley equation $\sigma - \sigma_c = \dot{\gamma}^k$ (where the steady-state flow rate is equal to the kth-root of the stress above the yield stress)[40]. We can compare our adhesive granular material model to this classical behaviour in the long-timescale limit by fitting the strain versus time to a curve (with fitting parameters A, B and $\tau_{\text{relax}} = 45$ simulation units) of the form: $\delta(t) = A + Bt(1 - e^{-t/\tau_{\text{relax}}})$ (Extended Data Fig. 7). By plotting the asymptote of the fit versus the fixed driving force, we find that the Herschel–Buckley equation is consistent with a $k \approx 3$ scaling (Fig. 3b(iv)).

To mimic the distributed activity of the organism induced by motility, we expand the distributed locomotion to lowest order in the devioric field[18]. These long-wavelength collective modes represent a low-order approximation to the dynamics of the forcing on this epithelial layer arising from distributed propulsion. This has the added benefit of serving as a control parameter for our driving away from equilibrium. By disentangling the dynamics from the distributed forcing, we

can more easily study the response of the model tissue to steady-state forcing. The functional form for this forcing takes the form of:

$$\nabla_x F \cdot \hat{x} = f_x$$

where we use f_x to characterize the amplitude of the gradient in the x-component of activity. The complete dynamics of this simple model combines the gradient of the disordered elasticity with this simplified activity to give us:

$$\gamma \frac{\mathrm{d}}{\mathrm{d}t}\begin{pmatrix} x_i \\ y_i \end{pmatrix} = \begin{pmatrix} \sum \nabla_{x_i} \epsilon_i \\ \sum \nabla_{y_i} \epsilon_i \end{pmatrix} + \begin{pmatrix} f_x x_i(t=0) \\ 0 \end{pmatrix}$$

We study the model under applied distributed propulsion coefficient f_x, beginning with a constant pull f_x followed by activity $f_x = 0$ after $t = T_{\mathrm{stop}}$. The response of the model is characterized as a function of f_x. We have also carried out complementary studies using a shear amplitude that qualitatively showed a similar behaviour (data not shown).

To classify the response of this material as a function of amplitude f_x, τ_{mature} and l_{break}, we developed a suite of microstate measurements to characterize the type of transformations incurred by driving it out of equilibrium. The first two measures are the types of transformations to the neighborhood matrix. In an STZ, a constraint broken is replaced with another locally. The local number of constraints does not change with an STZ. In contrast, an edge-forming transformation reduces the number of constraints and picks up the modes associated with a new edge. By counting the number of constraints locally, we can classify changes to the connectivity as either CCC or non-CCC (see Supplementary Information for further discussion). These technical definitions open the door to the characterization of the competition between fracture and flow.

In addition, we define the packing fraction using a Monte Carlo method for each configuration. We place 10^6 points randomly within the domain of the material asking if each is within a cell or within the boundary of the organism. The number which land inside a cell over the cardinality of the set landing in the cells unioned with those in the organism provides a calculation of the packing fraction. The parameter spaces (Fig. 3b and Extended Data Fig. 6) were generated by superimposing these three measures. Taking the practical definition of a 'brittle material' as one that overwhelmingly creates edges and of a 'ductile' material as one that overwhelmingly changes neighbours, we can characterize a crossover from ductile-like materials at high l_{break} (short τ_{mature}) to more brittle materials at low l_{break} (long τ_{mature}).

To study the role of the dynamic force landscape in the evolution of the connectivity, we made our amplitude dependent upon time, $f_x(t)$. The dynamics of this driving amplitude took the form of stochastic Langevin dynamics governed by the equation:

$$\gamma \frac{\partial}{\partial t} f_x(t) = -k_{\mathrm{effective}}(f_x(t) - f_{x,o}) + \xi(t)$$

With $\xi(t) = 2kT\gamma\delta(t - t')$ consistent with fluctuation–dissipation theorem. This mimics an overdamped particle in a harmonic well, with a characteristic timescale of response determined by the relaxation time of the system.

By driving our model tissue with this stochastic distributed driving, we can measure the accumulated morphodynamics attributed to this dynamic force landscape. We observe three central phenomena: fracture, STZs and healing. We wish to transfer our understanding to experiments where we do not have direct and error-free access to the microstate, so we sought to characterize the dynamics of transformation in a coarse-grained way using a metric from the granular matter literature, D^2_{min}. By comparing the signatures of high non-affine motion to known neighbourhood transformations, we extracted a threshold above which D^2_{min} is a good indicator of neighbourhood transformation (Fig. 3). We also used the model dynamics to characterize the sensitivity of these measurements to parameter selection, confirming best practices of choosing the interrogation radius consistent with the pair correlation function (Extended Data Fig. 9).

Computational analysis techniques. We used different computational analysis techniques to quantify the experimental time-lapse datasets. The dorsal-layer datasets with sticky microbeads tagging were visualized using Flowtrace[42], a simple tool for visualizing coherent structures in biological fluid flows (in ImageJ; http://imagej.nih.gov/ij/). The Flowtrace algorithm generates pathlines of particles with a given input projection time (here we chose 5 s).

The dorsal-layer sticky-microbead datasets were also analysed using the particle tracking technique in MATLAB (Mathworks; http://www.mathworks.com/). The first step involves image-processing operations such as background subtraction and spatial filtering to ensure that we can optimally identify the locations of the fluorescent 'blobs' of sticky microbeads for tracking. In the next step, the particles are tracked over time using the nearest-neighbour particle-tracking algorithm. The particle tracks are then stored for further data analysis.

Next, we studied the non-affine motion (non-uniform or disordered motion) of these tracked microbeads to measure the local amount of deviation in particle displacements from a linear strain field. Non-affine particle motion is a key feature in many soft matter systems such as amorphous solids[36], colloids[55], jammed materials[56], granular materials[57] and cell migration[58]. We quantified non-affine motion using the D^2_{min} metric[36] for all the tracked particles over a short timescale of 1 s. This D^2_{min} metric[36] minimizes the mean-squared difference between the actual displacements of the neighbouring particles relative to a central one and the relative displacements that they would have if they were in a region of uniform strain:

$$D^2(t, \Delta t) = \sum_n \sum_i ((r^i_n(t) - r^i_0(t)) - \sum_j (\delta_{ij} + \epsilon_{ij}) \times [r^j_n(t - \Delta t) - r^j_0(t - \Delta t)])^2$$

where, $r^i_n(t)$ is the ith component of the position of nth particles at time t. The uniform region of strain ϵ_{ij} that minimizes D^2 is then calculated according to Falk and Langer[36]. Then D^2_{min} is the minimum value of $D^2(t, \Delta t)$, which is the local deviation from affine deformation during the time interval $[t - \Delta t, t]$. The output of this metric is a squared length scale that quantifies the amount of disorder in the particle motion. The results are sensitive to the selected size of radius around the particles, and we have chosen optimal values of this parameter for our data analysis.

We used particle image velocimetry (PIV) analysis (PIVlab package[59] in MATLAB) to quantify the flow fields in the dorsal-layer sticky-microbeads time-lapse datasets in large width (13 mm × 13 mm square) confined PDMS milli-fluidic chips with variable fields-of-view. The animal is tracked manually for fixed durations, and the time-lapse recording is stopped when the field of view is changed. The PIV analysis is carried out for specific duration segments of these datasets where the field of view is fixed, and over short timescales (1 s). The image preprocessing step involves high-pass filtering, and we then carry out the PIV analysis by dividing the images into 64 × 64 pixel interrogation windows with 50% overlap on the first pass, and we use 32 × 32 pixel interrogation windows with 50% overlap for the second pass. Next, we select velocity threshold limits for post-processing the resulting velocity vector fields, smooth the data and use interpolation for missing vectors. We then calibrate the results, and calculate derived quantities such as the simple strain rate.

Data availability

The data that support the plots within this paper and other findings of this study are available from the corresponding author upon reasonable request.

Code availability

The computer codes used in this paper are available from the corresponding author upon reasonable request.

References

51. Farhadifar, R., Röper, J.-C., Aigouy, B., Eaton, S. & Jülicher, F. The influence of cell mechanics, cell-cell interactions, and proliferation on epithelial packing. *Curr. Biol.* **17**, 2095–2104 (2007).
52. Chen, J., Newhall, J., Xie, Z. R., Leckband, D. & Wu, Y. A computational model for kinetic studies of cadherin binding and clustering. *Biophys. J.* **111**, 1507–1518 (2016).
53. Razzell, W., Bustillo, M. E. & Zallen, J. A. The force-sensitive protein Ajuba regulates cell adhesion during epithelial morphogenesis. *J. Cell Biol.* **217**, 3715–3730 (2018).
54. Yap, A. S., Gomez, G. A. & Parton, R. G. Adherens junctions revisualized: organizing cadherins as nanoassemblies. *Dev. Cell* **35**, 12–20 (2015).
55. Chikkadi, V. & Schall, P. Nonaffine measures of particle displacements in sheared colloidal glasses. *Phys. Rev. E* **85**, 031402 (2012).
56. Keim, N. C. & Arratia, P. E. Mechanical and microscopic properties of the reversible plastic regime in a 2D jammed material. *Phys. Rev. Lett.* **112**, 028302 (2014).
57. Utter, B. & Behringer, R. P. Experimental measures of affine and nonaffine deformation in granular shear. *Phys. Rev. Lett.* **100**, 208302 (2008).
58. Lee, R. M., Kelley, D. H., Nordstrom, K. N., Ouellette, N. T. & Losert, W. Quantifying stretching and rearrangement in epithelial sheet migration. *New J. Phys.* **15**, 025036 (2013).
59. Thielicke, W. & Stamhuis, E. J. PIVlab—towards user-friendly, affordable and accurate digital particle image velocimetry in MATLAB. *J. Open Res. Softw.* **2**, e30 (2014).

Acknowledgements

We thank A. Bhargava and N. Eiseman for their contributions in the initial stages of the project, and S. Armon, P. Vyas, H. Soto-Montoya, W. Gilpin, H. Vaidehi Narayanan and members of the Prakash Lab at Stanford University for useful suggestions. We thank V. Chikkadi, S. Bandyopadhyay, S. Shekhar, N. Clarke and C. Lowe for helpful scientific discussions; K. Uhlinger for help with marine algae cultures; L. Buss for the generous gift of animals; R. Konte for help with the illustrations, C. Espenel, A. Khan and J. Mulholland (Cell Sciences Imaging Facility (CSIF), Stanford University) for help with microscopy. M.S.B. was supported by the National Science Foundation Graduate Research Fellowship (DGE-1147470) and the Stanford University BioX Fellows Program. This work was supported by NSF CCC grant (DBI-1548297) (M.P.), the CZI BioHub Investigator Program (M.P.) and the Howard Hughes Medical Institute (M.P.).

Author contributions

All authors designed the research. V.N.P. performed the experiments with assistance from M.S.B. and M.P.; V.N.P. and M.S.B. analysed the data; M.S.B. developed the theoretical framework and performed simulations. All authors wrote and reviewed the manuscript.

Competing interests

The authors declare no competing interests.

Additional information

Extended data is available for this paper at https://doi.org/10.1038/s41567-020-01134-7.

Supplementary information is available for this paper at https://doi.org/10.1038/s41567-020-01134-7.

Correspondence and requests for materials should be addressed to M.P.

Peer review information *Nature Physics* thanks Gijsje Koenderink and the other, anonymous, reviewer(s) for their contribution to the peer review of this work.

Reprints and permissions information is available at www.nature.com/reprints.

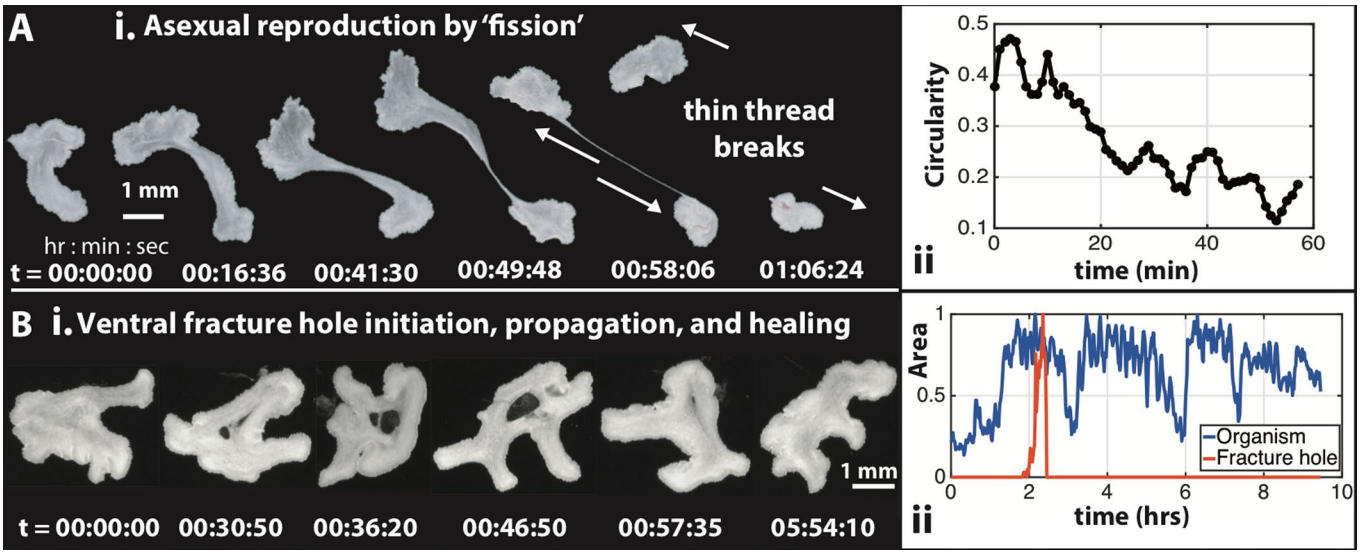

Extended Data Fig. 1 | Quantification of organismal shape change and area. A, (i) Time-lapse images of the asexual reproduction process; the animal changes shape from a more circular to an elongated shape. (ii) Quantification of these shape changes: Circularity (4π(Area)/(Perimeter^2)) decreases over time. **B**, (i) Time-lapse images of ventral epithelial fractures and healing; holes appear and disappear (heal). (ii) Quantification of organismal area and fracture hole area. The fracture hole (red) opens up for less than half an hour. The organismal area (blue) fluctuates due to the folding and unfolding of the animal, but the maximum value remains the same over ~10 hours, indicating that the growth timescales via cell division are much longer.

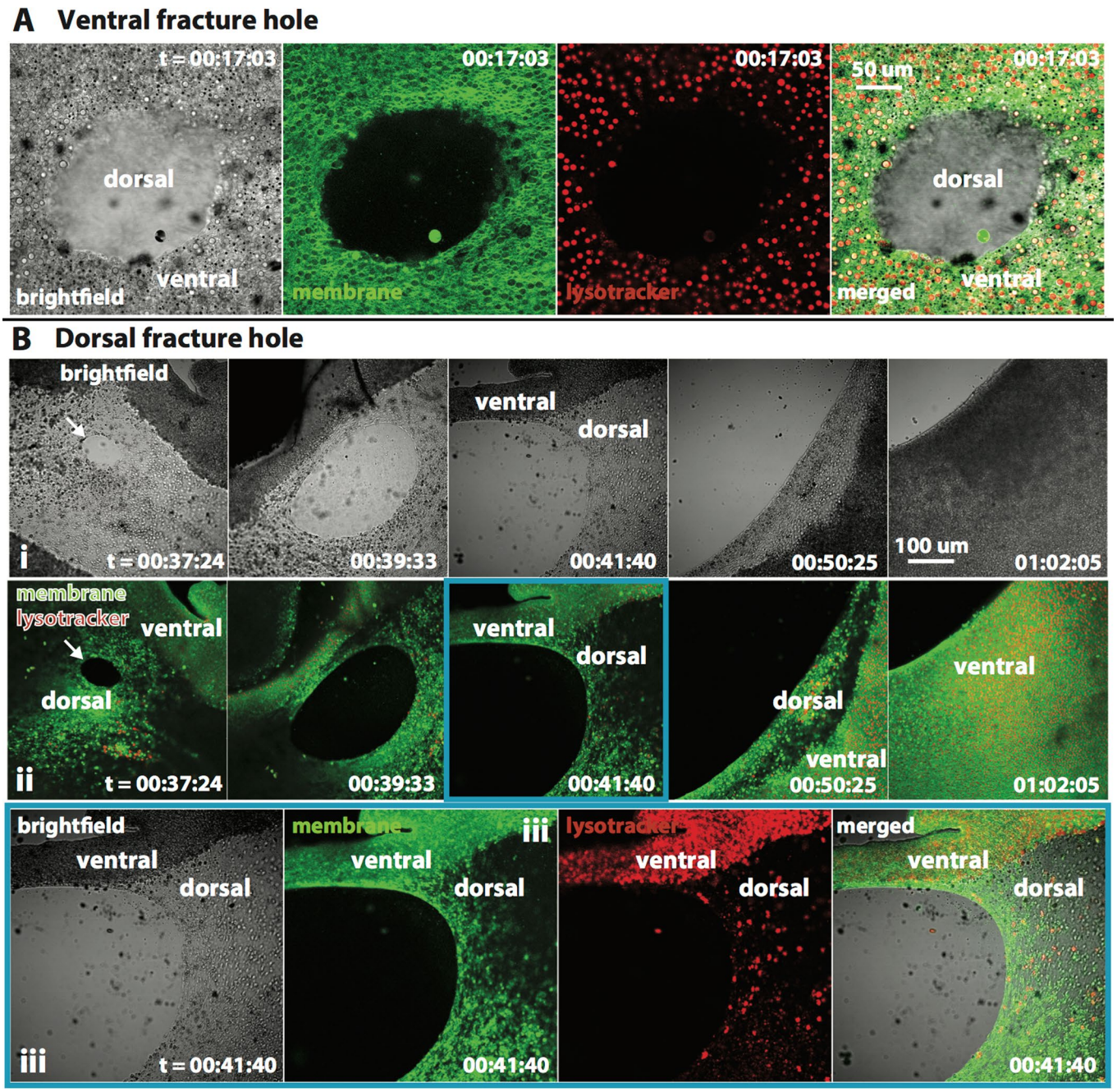

Extended Data Fig. 2 | Ventral and dorsal epithelial fractures in *T. adhaerens*. A, Ventral hole: All imaging channels corresponding to Fig. 2b (iv) are shown separately (cell membrane: green, acidic granules in lipophil cells: red). The bright-field channel reveals that the dorsal layer is still intact. **B**, Dorsal hole: (i) The brightfield channel corresponding to (ii) the dataset shown in Fig. 2d. (iii) All the imaging channels corresponding to third panel in (ii) are shown separately (cell membrane: green, acidic granules in lipophil cells: red). The dorsal fractures are through holes inside the bulk tissue of the animals. The ventral fracture event released broken fragments of ventral epithelial cells and lipophil cells (and their acidic granules), and since the dorsal epithelium is sticky, these granule fragments got stuck on the dorsal surface. This is the reason we see acidic granules on the dorsal epithelium in (iii).

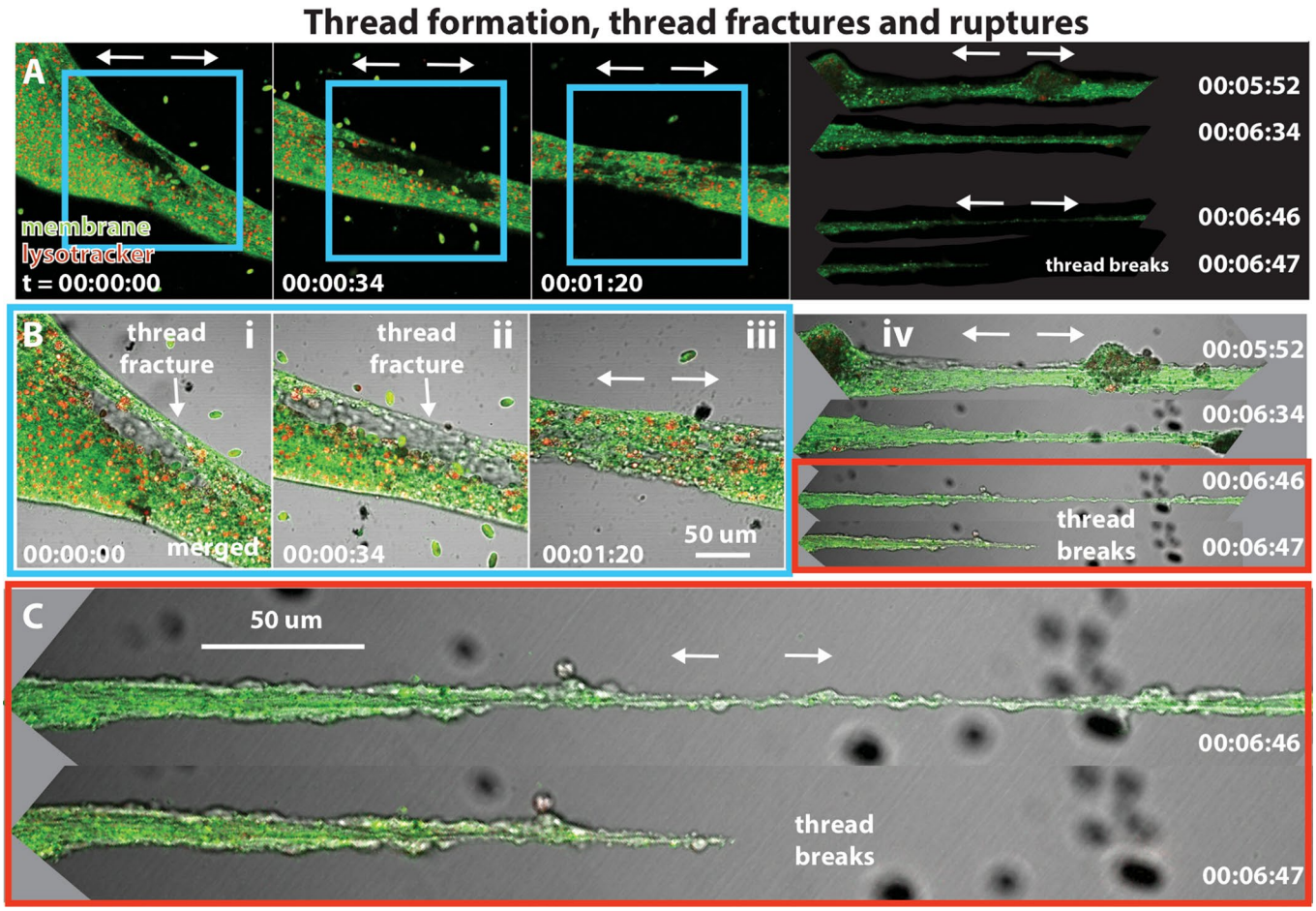

Extended Data Fig. 3 | Thread formation, thread fractures and ruptures. A, The stretched tissue between two regions of an animal that are pulling apart yield in a ductile fashion and form thread-like regions by undergoing local 'thread fractures'. Here, the subtle difference is in the location of fractures; ventral and dorsal epithelial fractures typically occur in the bulk, whereas these thread fractures occur on the edges. Functionally, these thread fractures are cumulative over time, resulting in rapid reduction (~ few min) in the cross-sectional area and lead to extremely thin (few cell layers thick) threads, which 'rupture' (~ few minutes) when pulled apart continuously. This mechanism plays an important part in the asexual reproduction process in these animals (Fig. 1b). **B**, Zoom-in versions of (A), with additional brightfield channel overlay on the images. **C**, Zoom-in version of panel in (B (iv)) highlighting breaking of the thread.

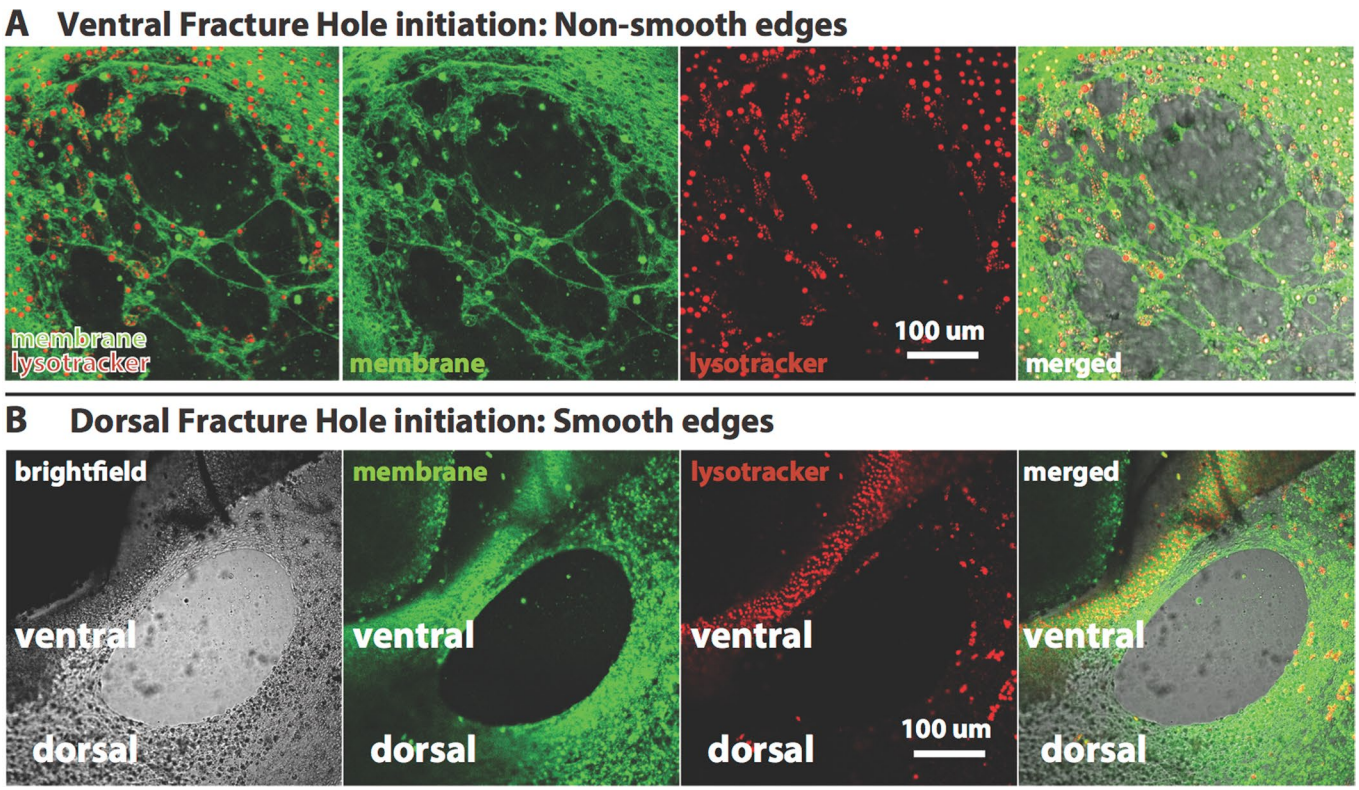

Extended Data Fig. 4 | Ventral and dorsal fracture hole initiation. A, Ventral fracture holes initiate as micro-fractures that coalesce to form larger holes, which are brittle-like with jagged edges and broken cellular fragments (The different imaging channels are shown separately). **B**, Dorsal fracture holes initiate as circular holes, which grow in size and remain smooth, indicative of a more ductile dorsal tissue (The different imaging channels are shown separately to facilitate comparison).

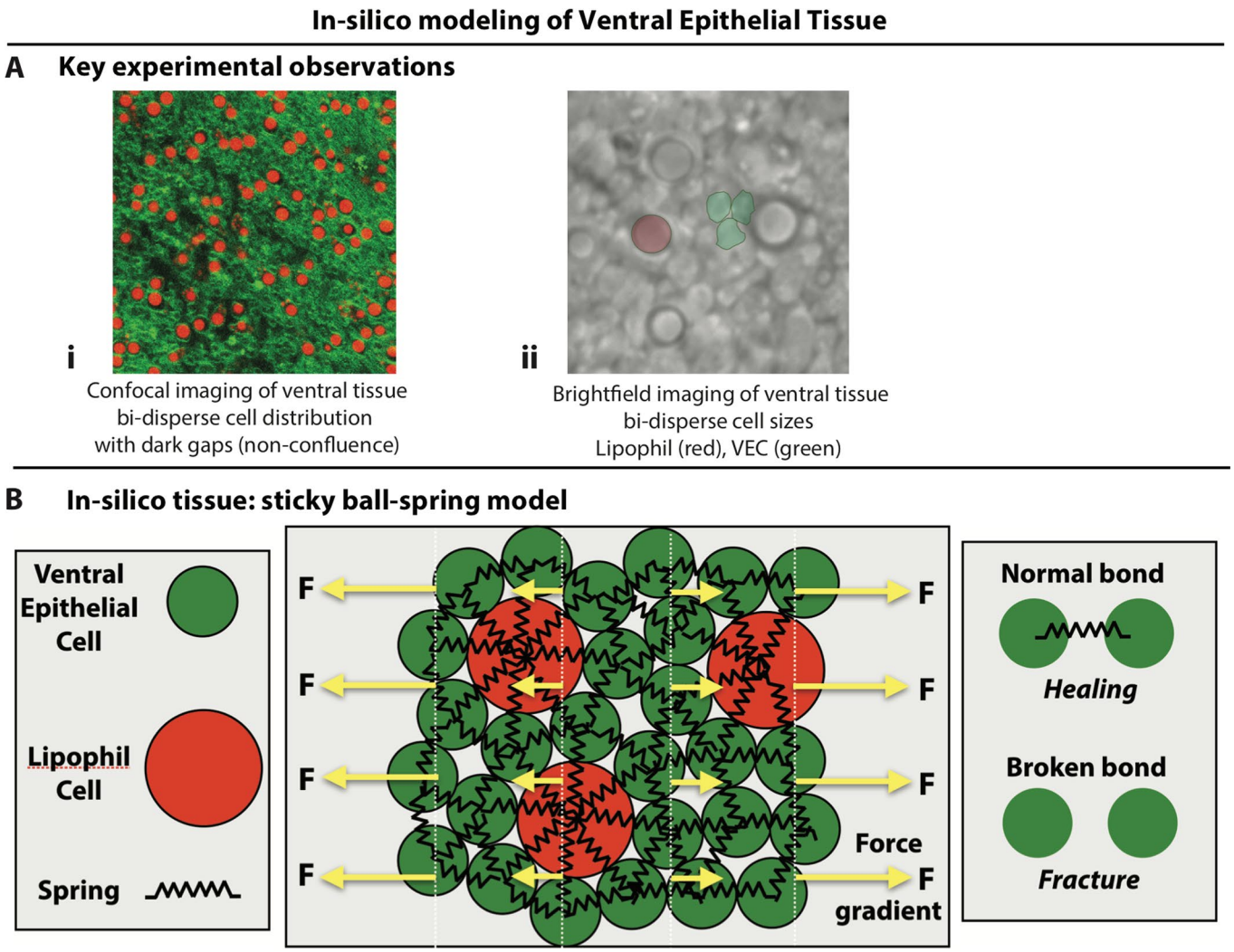

Extended Data Fig. 5 | Analysis of the metastable states. A, Key experimental observations: (i) Cells within the ventral layer are a bi-disperse mixture of ventral epithelial cells and lipophil cells. The tissue is also not perfectly confluent with gaps at the ventral surface. (ii) Digital zoom of brightfield 1 μm deep from the ventral surface shows bi-dispersity of cell sizes and shapes (lipophil cell - false colour red, and ventral epithelial cells (VEC) - green). **B**, Schematic cartoon illustration of model: chosen to simulate the experimentally observed bi-disperse mixture of ventral epithelial cells and lipophil cells shown in (A). The in-silico tissue model is a sticky ball-spring model, where the balls represent cells and the springs represent adhesion bonds between the cells.

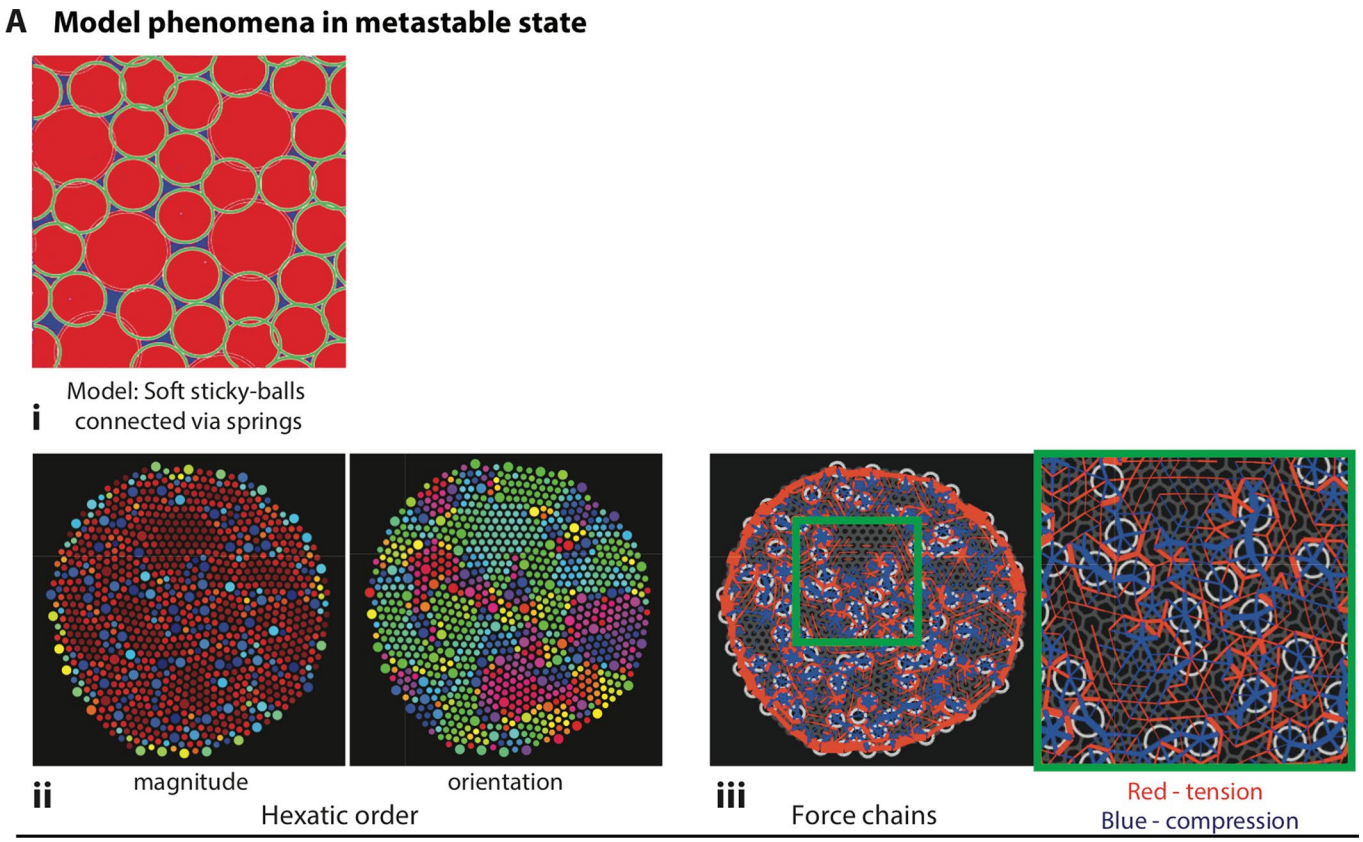

Extended Data Fig. 6 | (A) Model phenomena in metastable state. (i) Close up of a quenched state of the sticky-ball model where packing fraction is calculated with a simple Monte Carlo solver using blue colour regions between cells. (ii) Hexatic order - structural order measurement that reveals short range correlations of hexatic orientation for this bi-disperse system. (iii) Residual forces represented spatially through force chains demonstrates rich spatial heterogeneity at the metastable state. Thickness of force chains corresponds to magnitude with red representing force under tension and blue force under compression. **B**, Phase diagrams in metastable state: We explore a 2D cross-section of the model's parameter space with three diagnostic quantities: (i) 1 minus the packing fraction. (ii) Residual forces, and (iii) hexatic order. These phase spaces demonstrate how the metastable state properties can be tuned across a wide range of parameter configurations of bidispersity in the epithelial alloy, assuming that the results are independent of micro-configurations. We vary two parameters controlling tissue bidispersity: (i) % Larger cells, and (ii) Size ratio of large cells. In (i) we highlight three important cases (A, B and C) that we will consider in detail in the figures below.

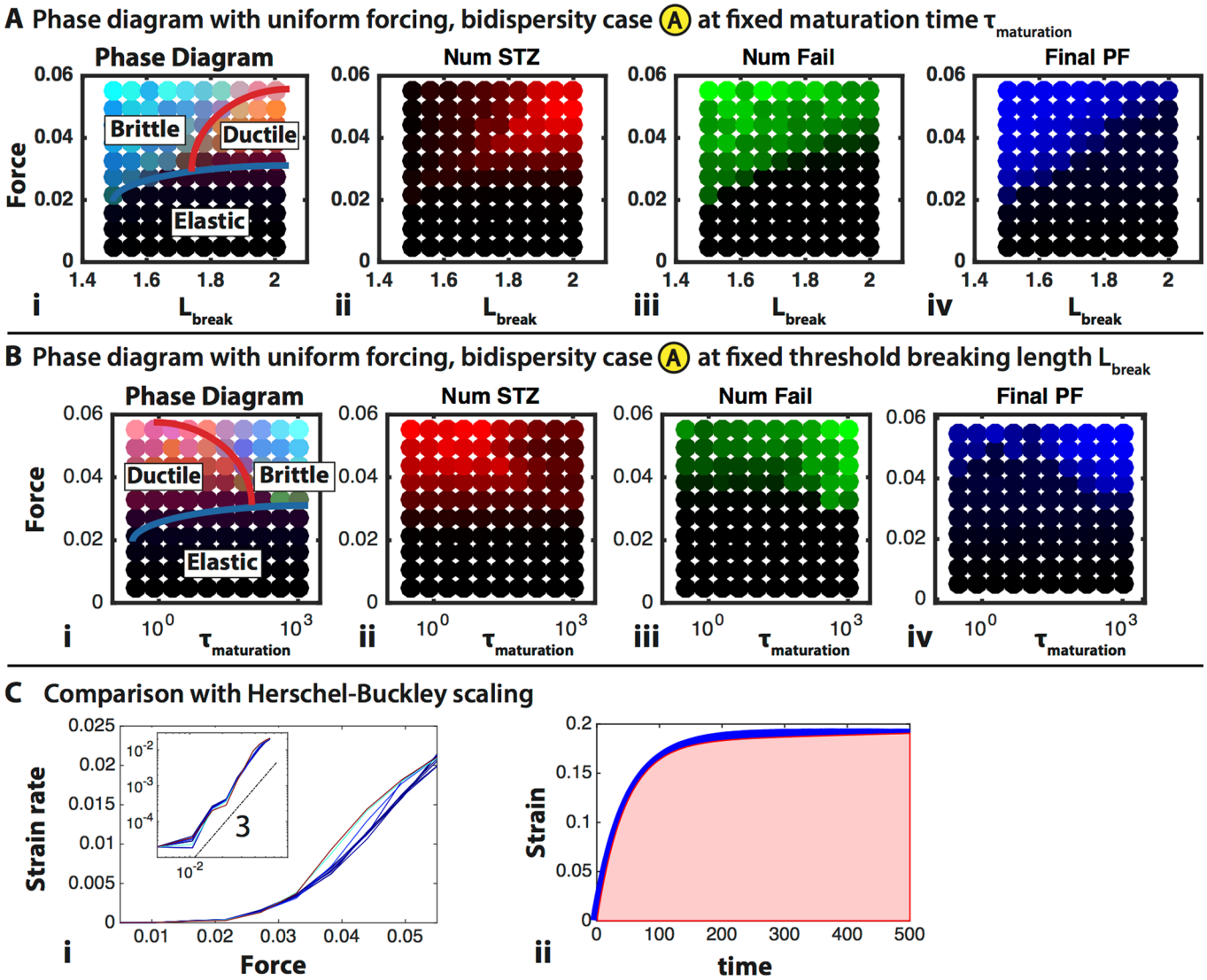

Extended Data Fig. 7 | Phase diagrams with uniform forcing. Pulling the heuristic model out of equilibrium for given parameters reveals two distinct behaviours: (i) a direct yielding through new edge formation and (ii) an intermediate yielding through reshuffling of the cell-cell junction network via higher order STZs. **A**, First, we consider the parameter of the maximum junctional length before failure, at fixed maturation time, and bi-dispersity case A from Extended Data Fig. 6B (12% larger cells, 1.7 size ratio). At small l_{break} the model yields to new edge formation at smaller loading. However, at a crossover ~ $l_{break} = 1.7$, for low loading gradients, the dominant yielding occurs through coordinated neighbour exchanges similar to STZs. This crossover value can be understood as the edge-forming energy exceeding the average STZ energy barrier (which is independent of l_{break}). The subsequent three panels in (A)ii-iv, are each one channel of the RGB parameter space displayed on the left. From left, red is the number of STZ transformations (or CCC), green is the number of edge forming transformations (or non-CCC), and blue is a helpful diagnostic, the packing fraction, for identifying holes within the tissue (light blue is low packing). **B**, Considering model tissues at different maturation times (at fixed threshold breaking length, and bi-dispersity case A from Extended Data Fig. 6B (12% larger cells, 1.7 size ratio) reveals a different crossover between a more ductile and a more brittle behaviour under distributed driving. At short maturation times, the formation of a new cell-cell junction is nearly instantaneous, so in a regime of $l_{break} = 1.95$, the yielding is driven through STZ-like (or CCC) transformations. However, when the maturation time reaches ~ 10x the dynamical timescale, the cell-cell junctions are too slow to reform and the tissue yields through new-edge formation and holes. This rapid de-lamination can be seen through the split channels (B)ii-iv in the reduction of STZs, the increase in new edges and the reduction of the packing fraction. **C**, To study the steady-state dependence of the model's Herschel-Buckley scaling on τ_{mature}, we complete a series of fits (ii) in the extension versus time curve. The asymptotic value of this fit represents the long-time behaviour of this yielding rate. Plotting the strain rate at steady-state versus the applied stress reveals a Herschel-Buckley-like relationship with a finite yield stress and a 3 scaling behaviour. Over the range explored τ_{mature} has only limited impact on the flow behaviour of this tissue.

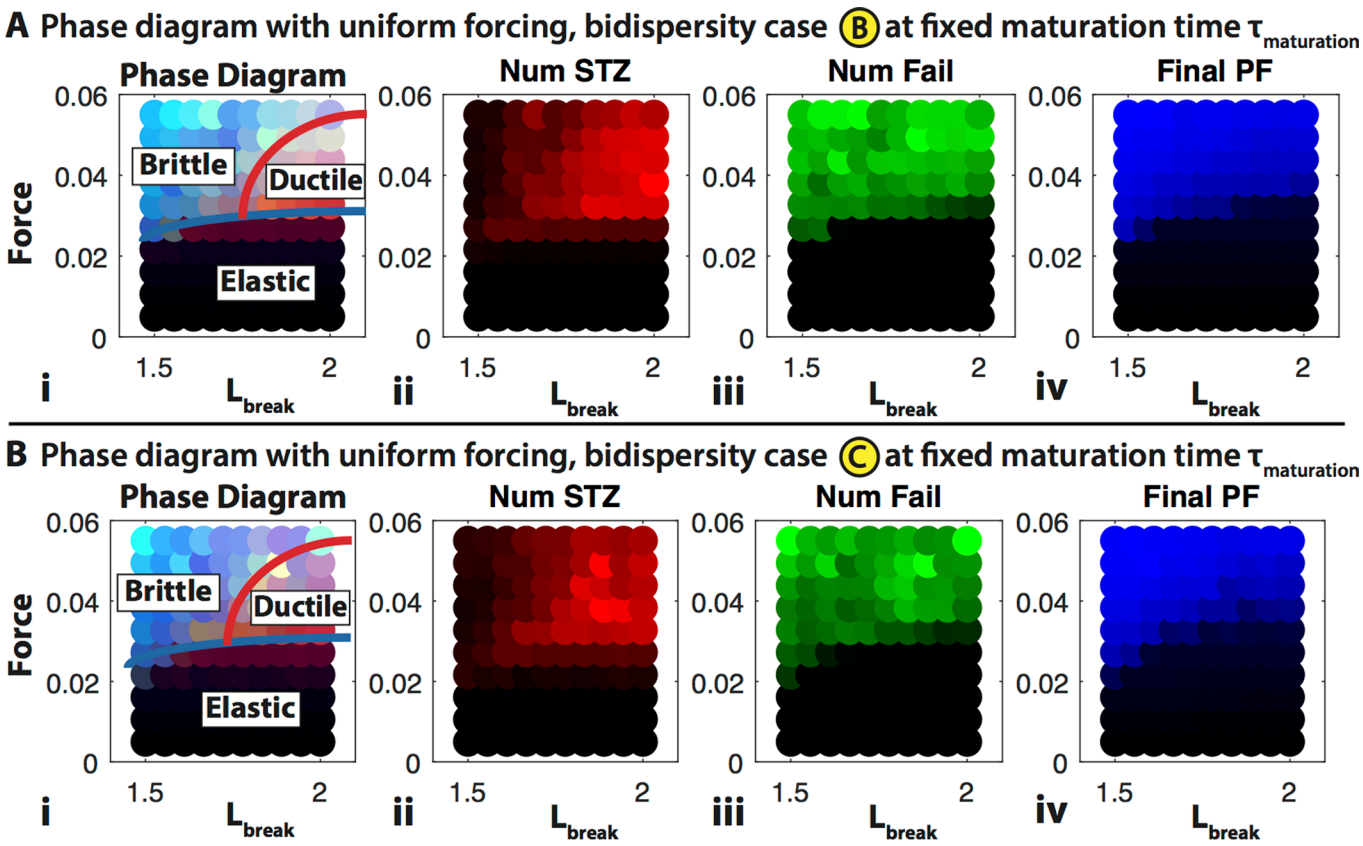

Extended Data Fig. 8 | Phase diagrams at different bi-dispersity cases. A, Case B from Extended Data Fig. 6B (12% larger cells, 1.1 size ratio), (B) case C from Extended Data Fig. 6B (6% larger cells, 2 size ratio). There are only subtle changes in the ductile–brittle transition at the different bi-dispersity cases.

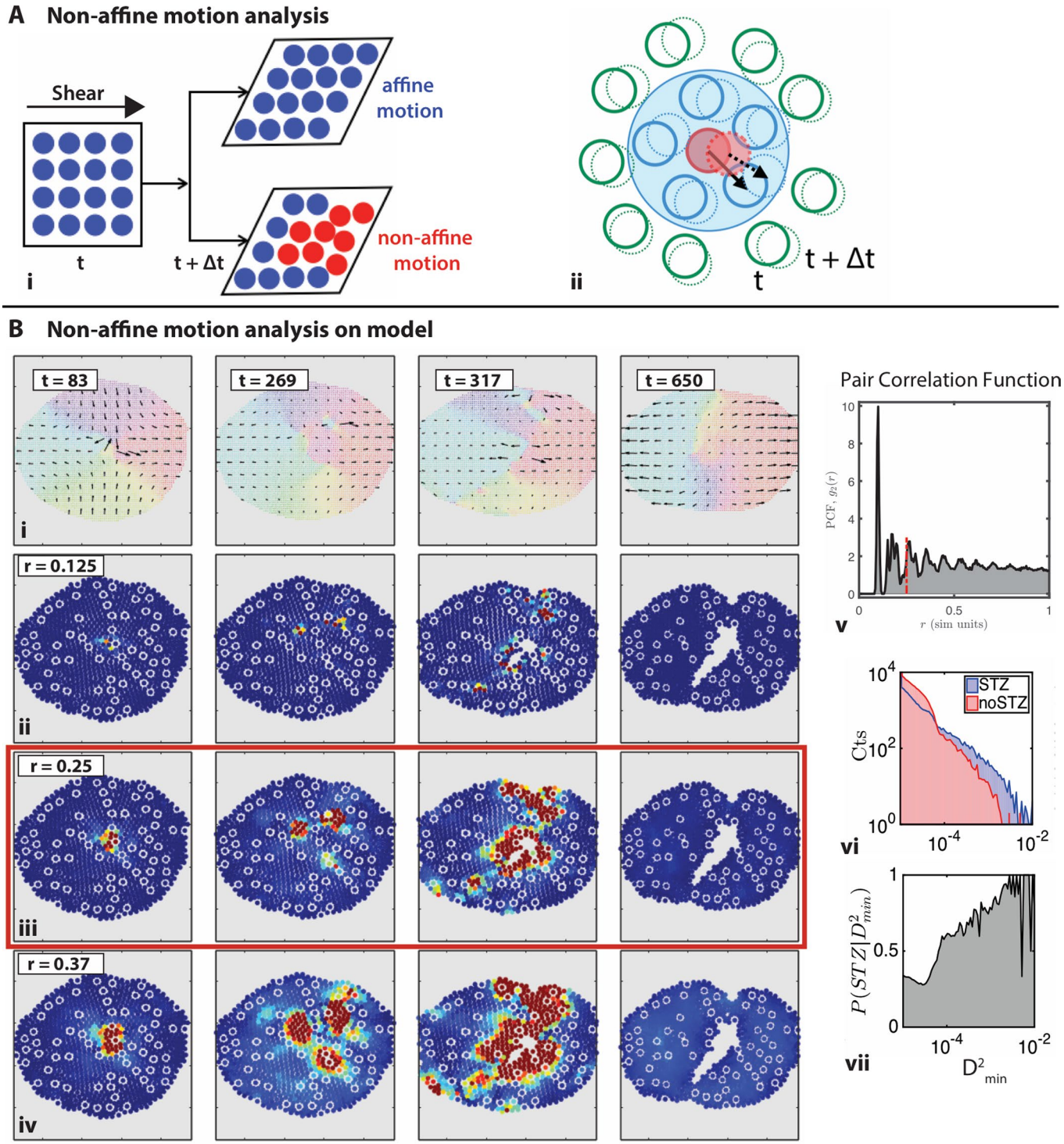

Extended Data Fig. 9 | Non-affine motion analysis. Leveraging the knowledge of the microstate in numerics to develop techniques for learning about the material properties of real tissue from experimental signatures. **A**, We employ a measure of non-affine motion called D^2_{min}. This measure subtracts actual motion of particles from the local affine transformation inferred from its neighbours' motion (ii). Large values of disagreement between actual motion and the affine projection are signaled in red (i). **B**,(i) We display the strain rate field calculated from interpolation of the displacements into a grid. Colour corresponds to orientation angle of the vector ranging from 0 to 2π. (B)(v) displays the pair correlation function showing rapid attenuation of the characteristic spacing over distances greater than 0.4 simulation units. The red dotted line signals the neighbourhood size used to calculate the metric in Fig. 3. Panels (B)(ii-iv) demonstrate the effect of the neighborhood size with with 50% variation on either side of that shown in the figure (B)(iii). Above is 50% smaller neighbourhood and below is 50% larger. The trade-off between sensitivity and spatial resolution is balanced by choosing the middle values B(iii). (B)(vi) shows the map between known simulation STZs and the measured D^2_{min}. B(vii) We find that this measure is a nice diagnostic for otherwise unobservable motions with 80% of the observed large $D^2_{min} \geq 10^{-3}$ corresponding to a known neighbourhood exchange via a STZ-like transformation.

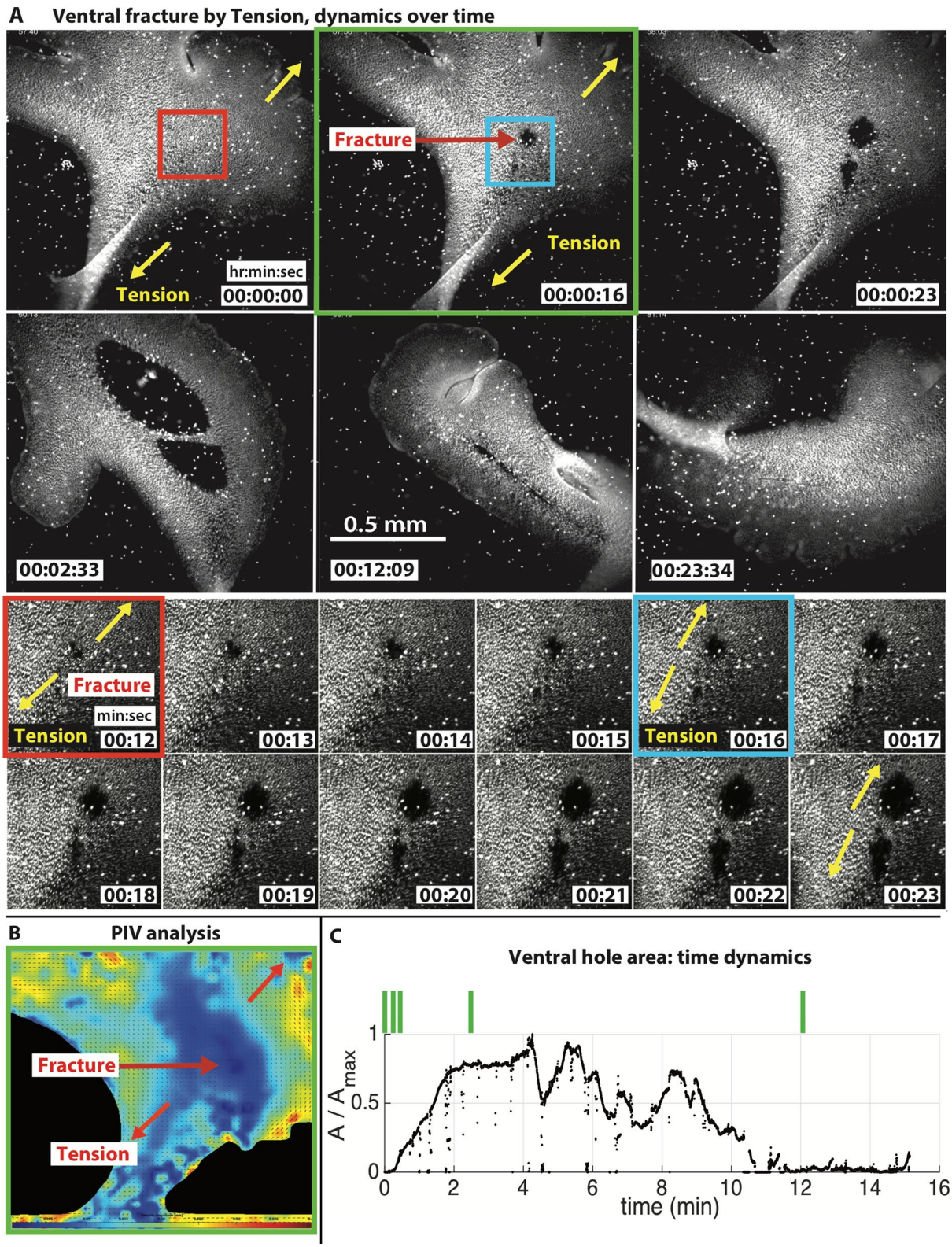

Extended Data Fig. 10 | Experimental time lapse images of tensile fractures. Here, we display more information on the same dataset as in Fig. 4(a). **A**, Time-lapse images showing the evolution of tensile-induced ventral fractures and their healing over a period of ~ 25 mins. **B**, PIV-derived velocity magnitude contours (with mean speed subtraction) of data in panel (A) at $t = 12s$. The fracture hole opens up in a dead velocity zone in the middle of the tissue being pulled from above and below - indicating a tensile force- induced fracture (blue color indicates zero velocity zones). **C**, Time-series plot of the fracture hole area in (A). The tension-induced fracture is an extremely fast process, with the hole reaching its maximum area in about 2 mins. The healing process is completed at about 12 mins. The green markers indicate timepoints corresponding to the snapshots displayed above.